Article

A discrete neuronal circuit induces a hibernation-like state in rodents

https://doi.org/10.1038/s41586-020-2163-6

Received: 27 June 2019

Accepted: 4 March 2020

Published online: 11 June 2020

Check for updates

Tohru M. Takahashi[1,2], Genshiro A. Sunagawa[3]✉, Shingo Soya[2], Manabu Abe[4,5], Katsuyasu Sakurai[2], Kiyomi Ishikawa[3], Masashi Yanagisawa[2], Hiroshi Hama[6], Emi Hasegawa[2], Atsushi Miyawaki[6], Kenji Sakimura[5], Masayo Takahashi[3] & Takeshi Sakurai[1,2,7]✉

Hibernating mammals actively lower their body temperature to reduce energy expenditure when facing food scarcity[1]. This ability to induce a hypometabolic state has evoked great interest owing to its potential medical benefits[2,3]. Here we show that a hypothalamic neuronal circuit in rodents induces a long-lasting hypothermic and hypometabolic state similar to hibernation. In this state, although body temperature and levels of oxygen consumption are kept very low, the ability to regulate metabolism still remains functional, as in hibernation[4]. There was no obvious damage to tissues and organs or abnormalities in behaviour after recovery from this state. Our findings could enable the development of a method to induce a hibernation-like state, which would have potential applications in non-hibernating mammalian species including humans.

Thermostatic animals expend a lot of energy for heat production to maintain their body temperature within a narrow range that is usually higher than the ambient temperature. Some mammals, however, actively lower their body temperature for energy conservation to survive food scarcity in winter—a state known as hibernation[1]. Laboratory mice (*Mus musculus*) do not hibernate, but they exhibit a short-term (less than 24-h) hypometabolic state known as daily torpor[5], during which reducing basal metabolism would be beneficial. Although several experiments have established that both daily torpor and hibernation are regulated by the central nervous system[4,6,7], the mechanisms involved remain unknown. The artificial induction of a hibernation-like hypometabolic state in non-hibernating animals, including humans, would be beneficial for many medical applications[2,3], as well as being of relevance to the possibility of long-distance space exploration in the future[8,9].

Induction of hypometabolism by Q neurons

A hypothalamic neuropeptide, pyroglutamylated RFamide peptide (QRFP), was originally identified using a bioinformatics approach[10,11] and reverse pharmacology[12]. Expression of *Qrfp* mRNA was found to be exclusively localized in the hypothalamus, in which it was distributed in the lateral hypothalamic area (LHA), tuber cinereum and the periventricular nucleus[12]. QRFP has previously been implicated in food intake, sympathetic regulation and anxiety[12,13]. We examined the function of neurons that produce QRFP using mice in which QRFP-producing neurons specifically express iCre (*Qrfp*^{iCre} mice) (Extended Data Fig. 1). We found that excitation of these neurons using a DREADDs (designer receptors exclusively activated by designer drugs) system[14] resulted in a long-lasting decrease in locomotor activity that started almost 30 min after intraperitoneal injection of clozapine-*N*-oxide (CNO) (a DREADD agonist). This effect coincided with a decrease in skin temperature in the interscapular area in which brown adipose tissue (BAT) is located (hereafter referred to as T_{BAT}) (Extended Data Fig. 2). We thus identified *Qrfp* as a genetic marker for hypothermia-inducing neurons. Although QRFP-producing neurons are exclusively located in the hypothalamus, they are distributed among several discrete hypothalamic regions[12] (Extended Data Fig. 1b, c). To identify the regions that were responsible for the effect, we manipulated iCre-positive neurons in these regions individually by injecting Cre-activatable adeno-associated virus (AAV) vectors[15] into the hypothalamus of *Qrfp*^{iCre} mice using several different stereotaxic coordinates. Injection of AAV into an anteromedial region of the hypothalamus resulted in the expression of designated genes such as *GFP* in iCre-positive neurons in the anteroventral periventricular nucleus (AVPe), medial preoptic area (MPA) and periventricular nucleus, but not in the LHA (Fig. 1a). We expressed hM3Dq–mCherry in these regions (that is, in the AVPe, MPA and periventricular nucleus) by injecting *Qrfp*^{iCre} mice with AAV_{10}-EF1a-DIO-hM3Dq-mCherry (Q-hM3D mice), and verified by in situ hybridization analysis that mCherry-positive cells expressed *Qrfp* mRNA (Extended Data Fig. 3a). Electrophysiological experiments confirmed that CNO strongly excited these mCherry-positive neurons (Extended Data Fig. 3b–e). We found that intraperitoneal injection of CNO in Q-hM3D mice led to more profound and stable states of hypothermia and immobility than those observed in *Qrfp*^{iCre}; *Rosa26*^{dreaddm3} mice (Fig. 1b, Supplementary Video 1). The hypothermic state, with very low T_{BAT} (below 30 °C), lasted for longer than 48 h. There were many neurons that were double-positive for mCherry and the neuronal activation marker FOS in the AVPe and MPA, confirming the excitation of these neurons in vivo by CNO (Fig. 1c). These observations suggest that iCre-positive neurons around the third ventricle—especially the neurons in the area of the AVPe and MPA (AVPe/MPA)

[1]Faculty of Medicine, University of Tsukuba, Tsukuba, Japan. [2]International Institute for Integrative Sleep Medicine (WPI-IIIS), University of Tsukuba, Tsukuba, Japan. [3]Laboratory for Retinal Regeneration, RIKEN Center for Biosystems Dynamics Research, Kobe, Japan. [4]Department of Cellular Neurobiology, Brain Research Institute, Niigata University, Niigata, Japan. [5]Department of Animal Model Development, Brain Research Institute, Niigata University, Niigata, Japan. [6]Laboratory for Cell Function Dynamics, RIKEN Center for Brain Science, Wako, Japan. [7]Life Science Center, Tsukuba Advanced Research Alliance (TARA), University of Tsukuba, Tsukuba, Japan. ✉e-mail: genshiro.sunagawa@riken.jp; sakurai.takeshi.gf@u.tsukuba.ac.jp

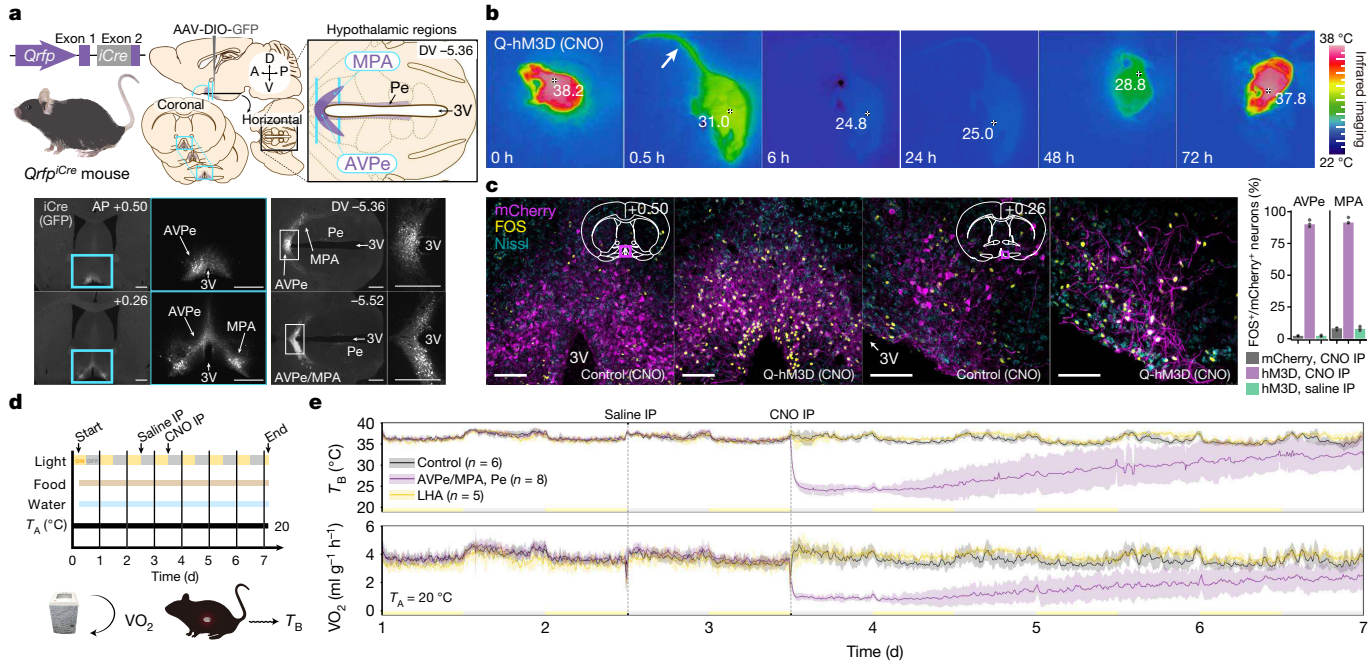

Fig. 1 | Activating *Qrfp*^{iCre} neurons in the hypothalamus lowers body temperature and energy expenditure. a, Distribution of Q neurons in *Qrfp*^{iCre} mice, visualized by GFP expression after injection of AAV_9-hSYN-DIO-GFP into the hypothalamic region. A, anterior; P, posterior; D, dorsal; V, ventral; Pe, periventricular nucleus; 3V, third ventricle. The purple fields in the modified stereotaxic brain maps (top) illustrate the locations of Q neurons that are around the third ventricle of the anterior part of the hypothalamus. In the bottom images, the boxed areas on the left are magnified on the right. Scale bars, 500 µm. **b**, Infrared thermal imaging of the surface body temperature of CNO-treated Q-hM3D mice. CNO was injected intraperitoneally at time 0 h. Tail temperature increased at 0.5 h (arrow). The ambient temperature was 23 °C. **c**, Left, brain images immunostained for a neuronal activation marker (FOS) 90 min after intraperitoneal (IP) injection of CNO in control and Q-hM3D mice (AP + 0.50 mm from bregma), and control and Q-hM3D mice (AP + 0.26 mm from bregma). Control mice were *Qrfp*^{iCre} mice that were injected with AAV_{10}-EF1α-DIO-mCherry into the AVPe/MPA. Scale bars, 100 µm. Right, bars show the median ratio of FOS-positive neurons in each group and dots represent the raw values of this ratio in each group. **d**, Schematic of metabolic analysis with chemogenetic activation of Q neurons in Q-hM3D mice. Intraperitoneal injection was performed at the beginning of the dark phase. T_A, ambient temperature. Yellow and grey boxes on the *y*-axis show light and dark phases, respectively. **e**, Temporal progression of hypothermia and hypometabolism after DREADD-mediated activation of Q neurons in Q-hM3D mice. T_B, body temperature. Purple, Q-hM3D mice; yellow, *Qrfp*^{iCre} mice with injection of AAV_{10}-EF1α-DIO-hM3Dq-mCherry in the LHA (to express hM3Dq in the LHA and tuber cinereum); black, control mice. Line and shading denote mean and s.d. of each group.

(quiescence-inducing neurons or 'Q neurons')—are mainly responsible for the induced hypothermic state.

We next implanted a telemetry temperature sensor in the abdominal cavity of Q-hM3D mice to monitor body temperature, and continuously assessed the metabolism of the mice by analysis of their respiratory gases (Fig. 1d). The results of this experiment confirmed that the CNO-induced hypothermic state in Q-hM3D mice was accompanied by a robust decrease in the rate of oxygen consumption (VO_2) (Fig. 1e), and that body temperature decreased concurrently with T_{BAT} after administration of CNO (Extended Data Fig. 4). DREADD-mediated excitation of iCre-positive neurons in the LHA and tuber cinereum in *Qrfp*^{iCre} mice did not induce hypothermia (Fig. 1e), suggesting that iCre-positive cells in lateral regions do not have a role in the effect.

During the state of Q-neuron-induced hypothermia and hypometabolism (QIH), the heart rate of mice decreased considerably, and the respiratory rate was reduced to a level undetectable by the method used, suggesting that the breathing of the mice was shallow (Extended Data Fig. 5a, b). Mice exhibited a very-low-amplitude electroencephalogram (EEG) during QIH, which differed from that observed in sleep (Extended Data Fig. 5b). Serum chemical data showed that blood glucose levels were lower than normal during QIH, presumably owing to decreased gluconeogenesis as a result of low sympathetic activity (Extended Data Fig. 5c).

Although DREADD-mediated effects usually last only a few hours after the injection of CNO[14], DREADD-induced QIH in Q-hM3D mice lasted for several days. At an ambient temperature of 20 °C, QIH (with a body temperature lower than 30 °C) lasted for longer than 48 h after only a single intraperitoneal injection of CNO (1 mg per kg body weight), and it took about a week for VO_2 to fully return to normal (Fig. 1e). During QIH, mice showed reduced locomotor activity and food intake, and body weight was lowest at one week after the induction of QIH, followed by a gradual recovery to the normal level (Extended Data Fig. 6a). We performed behavioural tests and found no difference between the group of mice in which QIH was induced and the control group of mice in any of the tests (Extended Data Fig. 6b–d). Gross histological examination of the brain, heart, kidney, liver and muscle did not reveal any damage to tissue after recovery from QIH (Extended Data Fig. 6e). QIH was reproducible in the same mice after repeated injections of CNO (Extended Data Fig. 6f).

Q neurons act on the dorsomedial hypothalamus

After expressing GFP specifically in Q neurons, we observed GFP-positive fibres in several regions of the hypothalamus and brain stem that are implicated in sympathetic regulation and in the control of body temperature[16] (Fig. 2a, Extended Data Fig. 7a–c). We first focused on the dorsomedial hypothalamus (DMH), which receives abundant Q neuron projections (Supplementary Video 2), and in which neurons that promote thermogenesis have previously been identified[17–19]. To examine the function of axonal projections from Q neurons to the DMH, we used an optogenetic approach. We expressed stabilized step function opsin (SSFO)[20] in Q neurons of mice (Q-SSFO mice), and first implanted optic fibres in the AVPe/MPA, where the cell bodies of Q neurons are found (Fig. 2b). Optogenetic excitation of SSFO–eYFP-positive cell bodies by

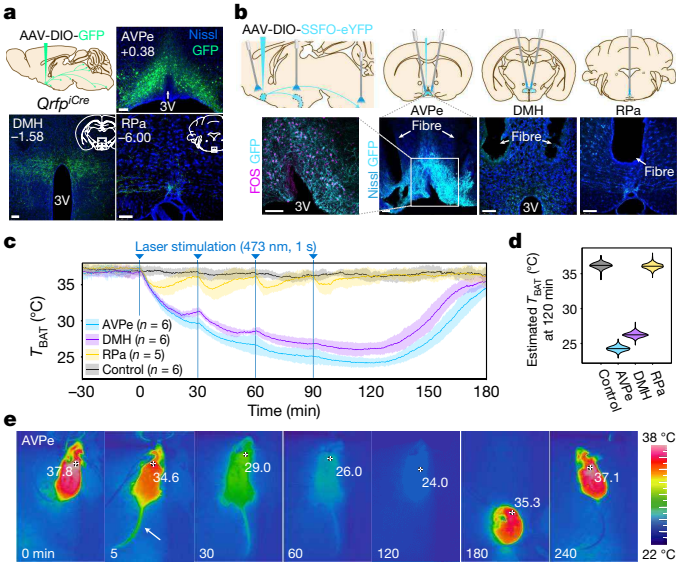

Fig. 2 | Histological and functional analyses of Q neuron projections. **a**, Distribution of cell bodies of Q neurons and a representative axon projection after expression of GFP in the AVPe/MPA. **b**, Strategy for optogenetic excitation of cell bodies or axons of Q neurons in the DMH and RPa. Scale bars, 100 μm (**a**, **b**). **c**, Change in T_{BAT} of Q-SSFO mice during optogenetic excitation of Q neurons. Laser stimulation is shown by blue arrowheads. Line and shading denote mean and s.d. of each group. **d**, The probability density of the estimated T_{BAT} at 30 min after the fourth laser shot. **e**, Representative thermographic images obtained by optogenetic activation of Q neurons (AVPe/MPA). Tail temperature increased at 5 min after the first laser stimulation (arrow).

applying a blue laser (473 nm; one light pulse of 1-s width) rapidly triggered robust hypothermia that lasted for about 30 min (Fig. 2c–e, Supplementary Video 3). Repeating the excitation of Q neurons every 30 min for 2 h resulted in more marked hypothermia, with T_{BAT} dropping to as low as the ambient temperature (22 °C). Many FOS-positive neurons were identified in SSFO–eYFP-positive cells in the AVPe/MPA after excitation (Fig. 2b). Optogenetically induced QIH lasted for less time than QIH that was induced chemogenetically, which suggests that Q neurons are highly sensitive for low levels of CNO or metabotropic signalling mediated by G_q in Q neurons has a role in the long-lasting nature of QIH.

Next, we implanted optic fibres bilaterally in the DMH of Q-SSFO mice and applied optogenetic excitation to the axonal fibres. This manipulation effectively decreased T_{BAT} (Fig. 2c). Optogenetic excitation of Q neuron fibres in the raphe pallidus nucleus (RPa) (Fig. 2b)—a region known to contain sympathetic premotor neurons for thermogenesis through BAT[21]—had subtle effects on T_{BAT} (Fig. 2c). Stimulation of both the cell bodies and the fibres of Q neurons in the DMH or the RPa caused a transient increase in tail temperature, which suggests that peripheral vasodilation is caused by stimulation that acts on both the DMH and the RPa (Extended Data Fig. 7d).

From these results, we postulate that Q neurons act mainly on the DMH (and to a smaller extent on the RPa) to induce QIH. To exclude the possibility that retrograde propagation of axonal excitation by optogenetic stimulation of DMH fibres resulted in the excitation of other collateral projections to induce the effect, we took advantage of the function of SSFO, which is deactivated by yellow light[20]. We found that deactivation of SSFO in the DMH immediately abolished the decrease in T_{BAT} (Extended Data Fig. 7e), further supporting the importance of the Q neuron projections to the DMH.

The thermoregulatory system during QIH

We observed an increase in temperature in the tails of mice immediately after the induction of QIH by either optogenetic or pharmacogenetic excitation of Q neurons. This suggests that peripheral vasodilation was triggered to release heat during the period of decreased body temperature (Figs. 1b, 2e, Extended Data Fig. 7d). The peripheral vasodilation without an increase in body temperature indicates that the reference body temperature (T_R), or the theoretical set-point of body temperature, was reset to a lower value than that in a normal state—a feature of hibernation[4]. To further investigate this possibility, we characterized the thermoregulatory system during QIH. When an animal is doing no external work and has a stable metabolism, the heat conductance (G), negative feedback gain of heat production (H), and T_R can be estimated from the body temperature and VO_2 at different ambient temperatures[5]. We recorded the body temperature and VO_2 of Q-hM3D mice during QIH at various ambient temperatures (8, 12, 16, 20, 24, 28 and 32 °C) (Fig. 3a). The average body temperature and VO_2 11 h after intraperitoneal injection of saline or CNO were used to estimate the values of G, H and T_R (Fig. 3b, c). The 89% highest-posterior-density interval (HPDI; hereafter, the 89% HPDI is indicated by two numbers in square brackets) of the heat conductance (G) was [0.212, 0.221] ml g^{-1} h^{-1} °C^{-1} in a normal state and [0.182, 0.220] ml g^{-1} h^{-1} °C^{-1} in QIH (Fig. 3d–f), suggesting that heat conductance is comparable under normal and QIH conditions. This differs from daily torpor, during which the value of G is lower than that observed in normal conditions[5]. For the negative feedback gain of heat production parameter (H), the 89% HDPI was [3.43, 8.72] ml g^{-1} h^{-1} °C^{-1} in a normal state and [0.181, 0.369] in QIH (Fig. 3g–i). This represents a 95.3% reduction in the median value of H in the QIH state compared to the normal state, suggesting a robust decrease in heat production. This decrease in H resembles the previously reported reduction of H during fasting-induced daily torpor (FIT)[5]. Notably, T_R was estimated to be [36.04, 36.60] °C in the normal condition and [26.83, 29.13] °C in QIH (Fig. 3g, j). The difference in the median T_R was 8.41 °C, and the posterior distribution of the difference (ΔT_R) was [7.18, 9.57] °C, demonstrating a reduction in T_R during QIH (Fig. 3k). Considering the very small shift in T_R that is observed in FIT[5], this observation underscores the similarity between QIH and hibernation and the difference between QIH and daily torpor—although we should note that T_R was estimated only in a narrow interval of ambient temperatures here, which is different from estimations in hibernators.

To provide more evidence of the reduction in T_R during QIH, which is a prominent characteristic of hibernation, we observed the relationship between the posture and metabolism of mice when the ambient temperature was changed during QIH (Fig. 3l, Extended Data Fig. 8a, b). Notably, at an ambient temperature of 28 °C, mice showed an extended posture during QIH—a posture that is normally seen in animals exposed to a hot environment (image D in Fig. 3l). This was different from the typical sitting posture that was observed during FIT at an ambient temperature of 28 °C (B in Fig. 3l). These observations further demonstrate that T_R was lower in QIH than in FIT or a normal state. Moreover, when the ambient temperature was lowered to 12 °C, the mouse returned to a sitting posture (E in Fig. 3l), exhibited shivering (Supplementary Video 4) and showed an increase in VO_2. These results support the hypothesis that during QIH, T_R is lowered, but bodily functions and behaviour are still regulated to adapt to a change in ambient temperature.

During QIH, mice showed a higher VO_2 when they were exposed to an ambient temperature below 16 °C compared with a temperature of 20 °C or 28 °C (Fig. 3b, Extended Data Fig. 8c). This shows the similarity between QIH and hibernation, in which mice showed an increased metabolism when the ambient temperature was lowered to a certain level[22]. This regulated hypometabolic feature of QIH was also confirmed in individual mice (Fig. 3l, Extended Data Fig. 8a, b). In addition, the respiratory quotient dropped to a level close to 0.7 at all ambient temperatures during QIH, implying that the energy source shifted from carbohydrates to lipids (Fig. 3l, Extended Data Fig. 8a). This agrees with the reduction in respiratory quotient that has been reported previously in deep torpor during hibernation[23]. The behavioural and metabolic responses of mice during QIH were quite different from

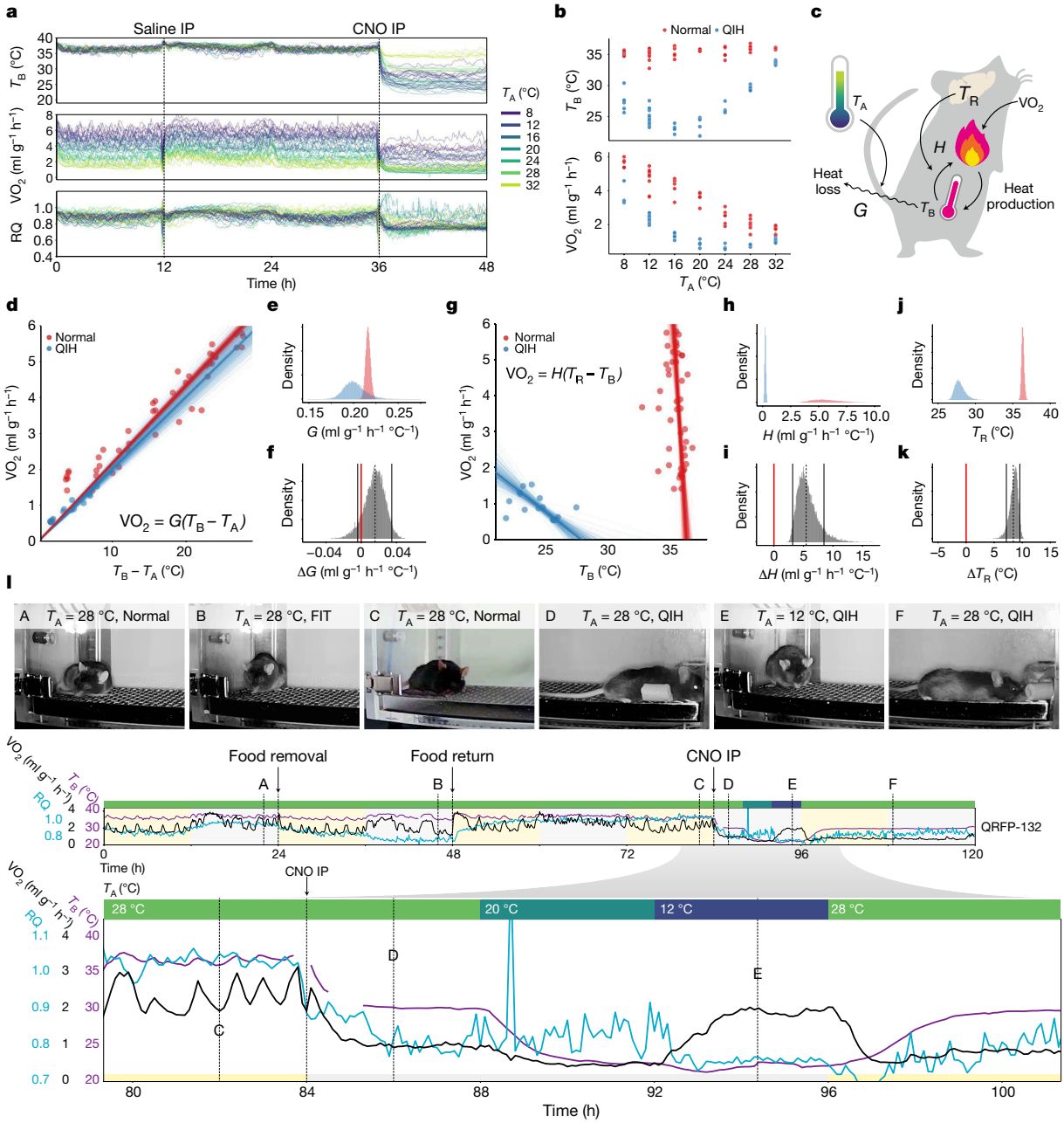

Fig. 3 | Q-neuron-induced hypometabolism is accompanied by a lowered set-point of body temperature. a, Change in body temperature, VO_2 and respiratory quotient (RQ) during QIH at various ambient temperatures. Each line denotes one mouse. **b**, Minimum body temperature (top) and VO_2 (bottom) under normal and QIH conditions. **c**, Schematic of heat-production and heat-loss pathways in mice. Heat loss is proportional to the difference between T_A and T_B at factor G. Heat production is governed by the difference between T_R and T_B at factor H. **d**, Relationship between $T_B - T_A$ and VO_2 at various values of T_A. The slope of the curve denotes G. Dots are recorded data, thick lines are drawn from the median of posterior G and thin lines are drawn from 500 randomly selected values of G from posterior samples. **e**, Posterior distribution of estimated G. **f**, Difference in G from QIH to the normal condition. **g**, Relationship between T_B and VO_2 at various values of T_A. The negative slope of the curves denotes H and the x-axis intercept denotes T_R. Dots and lines as in **d**. **h**, Posterior distribution of estimated H. **i**, Difference in H from QIH to the normal condition. **j**, Distribution of estimated T_R. **k**, Difference in T_R from QIH to the normal condition. **l**, Metabolic transition and postures during QIH within an individual mouse. The bottom chart is the timewise magnification of the top chart. The mouse shows a curled-up posture during FIT at $T_A = 28$ °C (B), but an extended posture during QIH at $T_A = 28$ °C (D). Even during QIH when T_A is lowered to 12 °C, the mouse assumes a curled-up posture, as in FIT (E), indicating that it is avoiding heat loss. During QIH, the respiratory quotient always decreases to a level close to 0.7, independent of T_A—a feature that is shared with hibernation. Three other examples are shown in Extended Data Fig. 8a.

those observed during a normal state, in which the primary function of the thermoregulatory system is to maintain the body temperature within a narrow range (Extended Data Fig. 8d). QIH is also completely different from an anaesthetized state, in which mice showed neither an increase of VO_2 nor a change in posture when exposed to low ambient temperature (Extended Data Fig. 9).

Neurotransmission in Q neurons

Expression of tetanus toxin light chain (TeTxLC) in mouse Q neurons (Q-TeTxLC mice) completely abolished the induction of QIH (Extended Data Fig. 10a, b), suggesting that SNARE-mediated neurotransmission in Q neurons is necessary for the induction of QIH. To ascertain

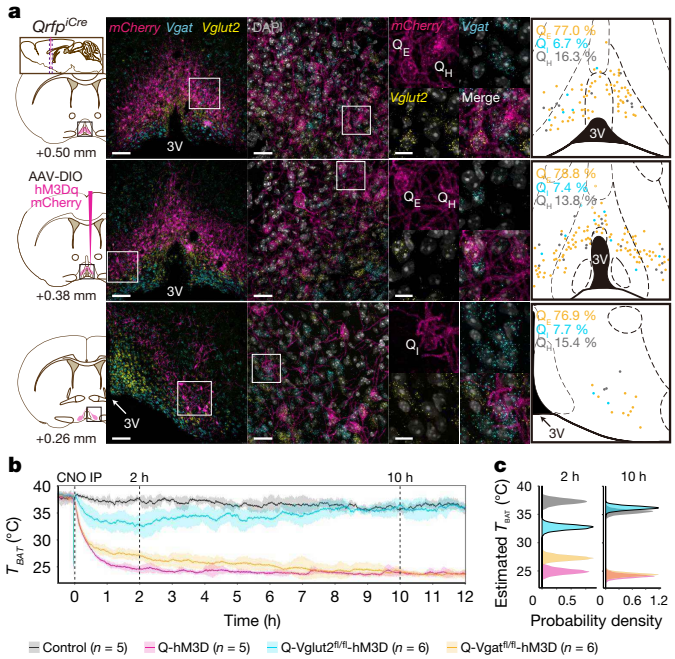

Fig. 4 | Glutamatergic and GABAergic neurotransmission of Q neurons are both involved in inducing QIH. a, In situ hybridization analysis showing Q neurons expressing *Vgat* and/or *Vglut2* in Q-hM3D mice. The left column shows schematics of coronal brain sections with positions from bregma. The middle images show the representative distribution of Q_E, Q_I and Q_H neurons. The right column shows the distribution of these neurons. We calculated the percentages of neurons in *mCherry*-expressing cells (counted on each coordinate from two slices prepared from independent Q-hM3D mouse brains) that were positive for *Vglut2* (Q_E; 315 out of 404 cells), *Vgat* (Q_I; 29 out of 404 cells) and both *Vglut2* and *Vgat* (Q_H; 60 out of 404 cells). Scale bars, 100 µm (left); 25 µm (middle); 10 µm (right). **b**, The absence of *Vgat* or *Vglut2* affects QIH. In Q-Vgat$^{fl/fl}$-hM3D mice (orange line), CNO injection effectively induced QIH, and T_{BAT} reached a level comparable to that observed during QIH in Q-hM3D mice (magenta line). In Q-Vglut2$^{fl/fl}$-hM3D mice (cyan line), the hypothermic effect of CNO injection was smaller and shorter. Line and shading denote mean and s.d. of each group. **c**, Estimated T_{BAT} of each genotype at 2 h and 10 h after CNO injection. Of note, T_{BAT} in Q-Vgat$^{fl/fl}$-hM3D mice showed little difference compared to that in Q-hM3D mice at 10 h after CNO injection, suggesting that glutamatergic neurotransmission from Q neurons is indispensable for maintaining a hypometabolic state in QIH.

whether Q neurons are inhibitory or excitatory, we examined the colocalization of *mCherry* expression with that of the genes that encode vesicular glutamate transporter 2 (VGLUT2) (*Vglut2*; also known as *Slc17a6*) and vesicular GABA transporter (VGAT) (*Vgat*; also known as *Slc32a1*) in Q-hM3D mice. We found that there are at least three populations of Q neurons: (i) Q_E (excitatory) neurons that are positive for *Vglut2* (77.9%); (ii) Q_I (inhibitory) neurons that are positive for *Vgat* (7.2%); and (iii) Q_H (hybrid) neurons that are positive for both *Vglut2* and *Vgat* (14.9%) (Fig. 4a). The proportions of these three populations were similar in all selected regions, and the neurons were intermingled with one another. Q_E neurons constitute the largest population, which is consistent with previous single-cell transcriptome studies of neurons of the preoptic area: in one report[24], 12 out of 31,299 cells were *Qrfp*-positive, and there were 7 excitatory and 4 inhibitory cells; and in another study[25], 16 out of 14,437 cells from the hypothalamus were *Qrfp*-positive, and there were 5 excitatory cells and 1 inhibitory cell.

Next, we mated *Qrfp*^{iCre} mice with *Slc32a1*$^{fl/fl}$ or *Slc17a6*$^{fl/fl}$ mice to obtain *Qrfp*^{iCre} mice that lack the expression of VGAT or VGLUT2 in Q neurons (which we term Q-Vgat$^{fl/fl}$ and Q-Vglut2$^{fl/fl}$ mice, respectively). After injecting AAV_{10}-EF1a-DIO-hM3Dq-mCherry into the AVPe/MPA (Q-Vgat$^{fl/fl}$-hM3D and Q-Vglut2$^{fl/fl}$-hM3D mice), we examined how the absence of VGAT or VGLUT2 affects QIH. In Q-Vgat$^{fl/fl}$-hM3D mice, injection of CNO effectively induced QIH, and T_{BAT} reached a level comparable to that observed during QIH in Q-hM3D mice (Fig. 4b, c). However, the initial reduction in T_{BAT} after injection of CNO was notably slower in these mice compared with that in control Q-hM3D mice. In Q-Vglut2$^{fl/fl}$-hM3D mice, although CNO injection induced a decrease in T_{BAT}, the effect was smaller and shorter than that in Q-hM3D mice. These results suggest that both glutamatergic and GABAergic neurotransmission cooperatively induce QIH.

Discussion

We have demonstrated that a hypothalamic population of neurons with a particular genetic identity (that is, expressing *Qrfp*) and spatial location (that is, within the AVPe/MPA) exists in mice, and that chemogenetic excitation of this population induces QIH—an extremely long-lasting state of regulated hypometabolism. QIH shares four key properties with hibernation. First, the hypothermic and hypometabolic state lasts for more than 24 h; second, the theoretical T_R is lowered but the thermoregulatory system remains functional—even under hypothermic conditions that are possibly harmful—to adapt to changes in the outer environment[4]; third, despite physiological functions being suppressed, with mice showing a slow heart rate, weak respiration, and low-voltage EEG, there is no tissue damage—a signature feature of hibernation[26]; and finally, mice spontaneously recover from QIH without any external manipulation.

By analysing the expression of FOS, a previous study showed that cells near the third ventricle are activated during hibernation in the thirteen-lined ground squirrel[27]. This activation pattern is similar to the region in which Q neurons are localized, suggesting that hibernators might also use Q neurons to induce hibernation. As the ability to hibernate exists among distantly related mammals—including rodents, the caniformia and even primates[28]—it is reasonable to hypothesize that the neuronal mechanism of hibernation is preserved among a broad range of mammalian species, although the system is not mobilized in non-hibernating species.

We identified the DMH as the major effector site of Q neurons. Glutamatergic DMH neurons located in the dorsal area of the DMH that send projections to the RPa have previously been shown to modulate BAT thermogenesis, which suggests that there is a connection between the DMH and the RPa[18,19]. A previous report showed that suspended animation in rats was induced by microinjection of muscimol into the RPa, which was accompanied by initial vasodilation in the tail[29]. These observations indicate that GABAergic neurotransmission by Q_I neurons might inhibit the circuit between glutamatergic DMH neurons and the RPa to induce tail vasodilation. Q_E neurons might excite another subset of DMH neurons to inhibit heat production. Future studies that identify QIH-inducing neurons in the DMH will enable the mechanism of QIH to be further elucidated.

The physiological role of Q neurons remains unknown. One possible function in which they are involved is the regulation of daily torpor. Although QIH is more similar to hibernation than to daily torpor, a shared mechanism might be present between hibernation and daily torpor[30]. In line with this, we found that the normal architecture of FIT was disrupted when neurotransmission of Q neurons was blocked in Q-TeTxLC mice (Extended Data Fig. 10c–f), suggesting that the function of Q neurons is necessary to evoke the rapid decrease of body temperature that occurs during FIT—although QRFP did not itself have a role in regulating FIT (Extended Data Fig. 10g). In addition, Q-TeTxLC mice showed less circadian fluctuation in body temperature than did control mice, which suggests that Q neurons might be involved in the circadian regulation of body temperature (Extended Data Fig. 10h). Q neurons receive input from the preoptic area and paraventricular hypothalamic nucleus (Extended Data Fig. 11a–c), indicating that they could receive circadian information from these regions of the

brain. Because Q neurons are localized along the third ventricle and their dendrites extend along the ependyma of the third ventricle and regions of nearby circumventricular organs (Fig. 1a), they might also sense humoral factors that are released by tanycytes and ependymal cells[31], or by factors in the cerebrospinal fluid. Our histological study also suggests that many Q neurons constitute a unique subpopulation of previously shown warm-sensitive neurons that co-express the neuropeptides BDNF and PACAP (BDNF/PACAP neurons) in the preoptic area[32] (Extended Data Fig. 11d, e).

We found that, notably, mice can enter a hibernation-like multi-day state of torpor by stimulating a defined neuronal population. Moreover, we observed that excitation of AVPe/MPA neurons, including Q neurons, also induced a QIH-like hypometabolic state in rats—a species that shows neither hibernation nor daily torpor (Extended Data Fig. 12). This induction of a hibernation-like condition in a non-hibernating mammal is a step forward in our understanding of the neuronal mechanisms of regulated hypometabolism, and will enable further investigation into how each tissue adopts a hibernation-like state. Furthermore, the future development of a method that enables the selective manipulation of Q neurons could provide a new approach through which a QIH-like state of synthetic hibernation could be induced in humans. This would have many potential clinical applications, including the reduction of systemic tissue damage following heart attacks or strokes, and the preservation of organs for transplants.

Online content

Any methods, additional references, Nature Research reporting summaries, source data, extended data, supplementary information, acknowledgements, peer review information; details of author contributions and competing interests; and statements of data and code availability are available at https://doi.org/10.1038/s41586-020-2163-6.

1. Geiser, F. Hibernation. *Curr. Biol*. **23**, R188–R193 (2013).
2. Melvin, R. G. & Andrews, M. T. Torpor induction in mammals: recent discoveries fueling new ideas. *Trends Endocrinol. Metab*. **20**, 490–498 (2009).
3. Bouma, H. R. et al. Induction of torpor: mimicking natural metabolic suppression for biomedical applications. *J. Cell. Physiol*. **227**, 1285–1290 (2012).
4. Jastroch, M. et al. Seasonal control of mammalian energy balance: recent advances in the understanding of daily torpor and hibernation. *J. Neuroendocrinol*. **28**, 12347 (2016).
5. Sunagawa, G. A. & Takahashi, M. Hypometabolism during daily torpor in mice is dominated by reduction in the sensitivity of the thermoregulatory system. *Sci. Rep*. **6**, 37011 (2016).
6. Vicent, M. A., Borre, E. D. & Swoap, S. J. Central activation of the A_1 adenosine receptor in fed mice recapitulates only some of the attributes of daily torpor. *J. Comp. Physiol. B* **187**, 835–845 (2017).
7. Hitrec, T. et al. Neural control of fasting-induced torpor in mice. *Sci. Rep*. **9**, 15462 (2019).
8. Griko, Y. & Regan, M. D. Synthetic torpor: a method for safely and practically transporting experimental animals aboard spaceflight missions to deep space. *Life Sci. Space Res*. **16**, 101–107 (2018).
9. Choukèr, A., Bereiter-Hahn, J., Singer, D. & Heldmaier, G. Hibernating astronauts—science or fiction? *Pflugers Arch*. **471**, 819–828 (2019).
10. Fukusumi, S. et al. A new peptidic ligand and its receptor regulating adrenal function in rats. *J. Biol. Chem*. **278**, 46387–46395 (2003).
11. Chartrel, N. et al. Identification of 26RFa, a hypothalamic neuropeptide of the RFamide peptide family with orexigenic activity. *Proc. Natl Acad. Sci. USA* **100**, 15247–15252 (2003).
12. Takayasu, S. et al. A neuropeptide ligand of the G protein-coupled receptor GPR103 regulates feeding, behavioral arousal, and blood pressure in mice. *Proc. Natl Acad. Sci. USA* **103**, 7438–7443 (2006).
13. Okamoto, K. et al. QRFP-deficient mice are hypophagic, lean, hypoactive and exhibit increased anxiety-like behavior. *PLoS ONE* **11**, e0164716 (2016).
14. Roth, B. L. DREADDs for neuroscientists. *Neuron* **89**, 683–694 (2016).
15. Atasoy, D., Aponte, Y., Su, H. H. & Sternson, S. M. A FLEX switch targets channelrhodopsin-2 to multiple cell types for imaging and long-range circuit mapping. *J. Neurosci*. **28**, 7025–7030 (2008).
16. Nakamura, K. Central circuitries for body temperature regulation and fever. *Am. J. Physiol. Regul. Integr. Comp. Physiol*. **301**, R1207–R1228 (2011).
17. Zhao, Z.-D. et al. A hypothalamic circuit that controls body temperature. *Proc. Natl Acad. Sci. USA* **114**, 2042–2047 (2017).
18. Machado, N. L. S. et al. A glutamatergic hypothalamomedullary circuit mediates thermogenesis, but not heat conservation, during stress-induced hyperthermia. *Curr. Biol*. **28**, 2291–2301 (2018).
19. Piñol, R. A. et al. *Brs3* neurons in the mouse dorsomedial hypothalamus regulate body temperature, energy expenditure, and heart rate, but not food intake. *Nat. Neurosci*. **21**, 1530–1540 (2018).
20. Yizhar, O. et al. Neocortical excitation/inhibition balance in information processing and social dysfunction. *Nature* **477**, 171–178 (2011).
21. Morrison, S. F. Central control of body temperature. *F1000Res*. **5**, 880 (2016).
22. Ortmann, S. & Heldmaier, G. Regulation of body temperature and energy requirements of hibernating alpine marmots (*Marmota marmota*). *Am. J. Physiol. Regul. Integr. Comp. Physiol*. **278**, R698–R704 (2000).
23. Snapp, B. D. & Heller, H. C. Suppression of metabolism during hibernation in ground squirrels (*Citellus lateralis*). *Physiol. Zool*. **54**, 297–307 (1981).
24. Moffitt, J. R. et al. Molecular, spatial, and functional single-cell profiling of the hypothalamic preoptic region. *Science* **362**, eaau5324 (2018).
25. Chen, R., Wu, X., Jiang, L. & Zhang, Y. Single-cell RNA-seq reveals hypothalamic cell diversity. *Cell Rep*. **18**, 3227–3241 (2017).
26. Walker, J. M., Glotzbach, S. F., Berger, R. J. & Heller, H. C. Sleep and hibernation in ground squirrels (*Citellus* spp): electrophysiological observations. *Am. J. Physiol. Integr. Comp. Physiol*. **233**, R213–R221 (1977).
27. Bratincsák, A. et al. Spatial and temporal activation of brain regions in hibernation: *c-fos* expression during the hibernation bout in thirteen-lined ground squirrel. *J. Comp. Neurol*. **505**, 443–458 (2007).
28. Dausmann, K. H., Glos, J., Ganzhorn, J. U. & Heldmaier, G. Physiology: hibernation in a tropical primate. *Nature* **429**, 825–826 (2004).
29. Cerri, M. et al. The inhibition of neurons in the central nervous pathways for thermoregulatory cold defense induces a suspended animation state in the rat. *J. Neurosci*. **33**, 2984–2993 (2013).
30. Heldmaier, G., Ortmann, S. & Elvert, R. Natural hypometabolism during hibernation and daily torpor in mammals. *Respir. Physiol. Neurobiol*. **141**, 317–329 (2004).
31. Oomura, Y. et al. A new brain glucosensor and its physiological significance. *Am. J. Clin. Nutr*. **55**, 278S–282S (1992).
32. Tan, C. L. et al. Warm-sensitive neurons that control body temperature. *Cell* **167**, 47–59 (2016).

Methods

Data reporting

No statistical methods were used to predetermine sample size. The experiments were not randomized, and the investigators were not blinded to allocation during experiments and outcome assessment.

Animals

All animal experiments were performed at the International Institute of Integrative Sleep Medicine (IIIS), Tsukuba University and RIKEN Center for Biosystems Dynamics Research (BDR), according to their guidelines for animal experiments. They were approved by the animal experiment committees of each institute, and thus were in accordance with NIH guidelines. Except during torpor-inducing experiments, animals were given food and water ad libitum and maintained at an ambient temperature of 23 °C at IIIS and 22 °C at BDR and a relative humidity of 50%, with a 12-h light/12-h dark cycle. Because we found that mice that weighed more than 34 g did not reproducibly exhibit FIT, we excluded mice heavier than 34 g in daily torpor experiments.

Qrfp^{iCre} mice were generated by homologous recombination in C57BL/6N embryonic stem cells and implantation in 8-cell-stage embryos (ICR). A targeting vector was designed to replace the entire coding region of the *prepro-Qrfp* sequence in exon 2 of the *Qrfp* gene with *iCre* and a pgk-Neo cassette so that the endogenous *Qrfp* promoter drives expression of *iCre* (Extended Data Fig. 1). Chimeric mice were crossed with C57BL/6J females (Jackson Laboratory). The Pgk-Neo cassette was deleted by crossing the mice with FLP66 mice, which had been backcrossed to C57BL/6J mice at least 10 times. Initially, F_1 hybrids from mating heterozygotes with heterozygotes were generated. We backcrossed them to C57BL/6J mice at least 8 times. All experiments were performed on *iCre* heterozygotes, unless indicated otherwise. *Rosa26*^{dreaddm3} and *Rosa26*^{dreaddm4} mice were generated by homologous recombination in C57BL/6N embryonic stem cells, followed by the same procedure as in *Qrfp*^{iCre} mice, as described above. Targeting vectors are shown in Extended Data Fig. 2a. *Slc32a1*^{tm1Lowl} (referred to as *Vgat*$^{fl/fl}$) mice and *Slc17a6*^{tm1Lowl} (*Vglut2*$^{fl/fl}$) mice were obtained from the Jackson Laboratory (stock no. 012897 and 012898, respectively). Wistar rats were purchased from Oriental Yeast Co.

Viruses

AAVs were produced using a triple-transfection, helper-free method as previously described[33]. The final purified viruses were stored at −80 °C. Titres of recombinant AAV vectors were determined by quantitative PCR: AAV_{10}-EF1α-DIO-TVA-mCherry, 4×10^{13}; AAV_{10}-CAG-DIO-RG, 1×10^{13}; AAV_{10}-EF1α-DIO-hM3Dq-mCherry, 1.64×10^{12}; AAV_{10}-EF1α-DIO-mCherry, 1.44×10^{12}; AAV_{10}-EF1α-DIO-SSFO-EYFP, 1.35×10^{12}; AAV_9-SYN-DIO-TeTxLC-GFP, 6.24×10^{14}; AAV_9-hSYN-DIO-GFP, 4×10^{12}; AAV_{10}-CaMKIIα-hM3Dq-mCherry, 1.4×10^{14}; AAV_9-hSYN-DIO-GCaMP6 s, 1×10^{15} genome copies per ml. Recombinant rabies vectors were produced by a previously reported procedure[34,35]. The titre of SADΔG-GFP(EnvA) was 4.2×10^8 infectious units per ml.

Surgery

For injection of AAV vectors, male *Qrfp*^{iCre} heterozygous mice (8–12 weeks old) and male Wistar rats (8 weeks old) were anaesthetized with isoflurane and positioned in a stereotaxic frame (David Kopf Instruments). Virus was delivered into the target site at a controlled rate of 0.1 µl per min using a Hamilton needle syringe. The needle was kept in place for 10 min after injection. The waiting period for recovery and virus expression for the experiments was at least 2 weeks except as noted.

For the chemogenetic manipulation in Fig. 1, *Qrfp*^{iCre} mice underwent injection of AAV_{10}-EF1α-DIO-hM3Dq-mCherry into the hypothalamus (to express in the AVPe/MPA: anterior–posterior (AP), −0.22 mm; medial–lateral (ML), ± 0.25 mm; dorsal–ventral (DV), −5.50 mm; 0.50 µl in each site; to express in the LHA: AP, −1.00 mm; ML, ± 1.00 mm; DV, −5.00 mm; 0.30 µl in each site).

For the identification of the distribution and the axonal projections of Q neurons in Figs. 1, 2, we injected 0.30 µl AAV_9-hSYN-DIO-GFP into the hypothalamus (AVPe/MPA: AP, −0.22 mm; ML, 0.25 mm; DV, −5.50 mm) unilaterally.

For the optogenetic manipulations in Fig. 2 and Extended Data Fig. 7, we injected 0.3 µl AAV_{10}-EF1α-DIO-SSFO-EYFP into the AVPe/MPA (AP, 0.38 mm; ML, 0.25 mm; DV, −5.25 mm from bregma) unilaterally. Optical fibres were then implanted bilaterally above the AVPe/MPA (AP, 0.38 mm; ML, ± 0.25 mm; DV, −5.00 mm), bilaterally above the DMH (AP, −1.70 mm; ML, ± 0.25 mm; DV, −4.75 mm) or unilaterally above the RPa (AP, −6.00 mm; ML, 0.00 mm; DV, −5.50 mm). After a recovery period of at least three weeks in individual cages after injection, mice were subjected to infrared thermal-imaging experiments. Behavioural data were only included if these viruses were targeted specifically to Q neurons and the fibre-optic implants were precisely placed.

For demonstrating the identity and detailed anatomical location of Q neurons (Fig. 4a, Extended Data Fig. 11) and chemogenetic manipulation of conditional knockout mice (Fig. 4b), we injected 0.20 µl AAV_{10}-EF1a-DIO-hM3Dq-mCherry into the AVPe/MPA (AP, 0.38 mm; ML, 0.25 mm; DV, −5.25 mm from bregma) unilaterally.

For silencing experiments, we injected mixed AAV (0.20 µl AAV_9-SYN-DIO-TeTxLC-GFP and 0.20 µl AAV_{10}-EF1α-DIO-hM3Dq-mCherry) into the AVPe/MPA and periventricular nucleus region (AP, −0.22 mm; ML, ± 0.25 mm; DV, −5.50 mm) bilaterally (Extended Data Fig. 10a, b), and we injected 0.30 µl AAV_9-SYN-DIO-TeTxLC-GFP into the same injection sites (Extended Data Fig. 10c–g).

For rat experiments in Extended Data Fig. 12, we injected 0.20 µl AAV_{10}-CaMKIIα-hM3Dq-mCherry into the AVPe/MPA (AP, 0.12 mm; ML, ± 0.40 mm; DV, −8.50 mm from bregma) bilaterally.

Drug administration

CNO (Abcam, ab141704) was dissolved in normal saline at a dose of 100 µg ml^{-1} and frozen at −20 °C. The CNO solution was thawed on site, and it was administered intraperitoneally at a dose of 1 mg kg^{-1} for mice and 5 mg kg^{-1} for rats.

Biological signal recordings

For thermographic analysis, mice were put in experimental cages (25 × 15 × 10 cm) and monitored using an infrared thermal-imaging camera (InfReC R500EX, Nippon Avionics) positioned 30 cm above the cage floor. To clearly detect surface temperature, the back hair was removed with hair clippers one day before starting the experiment. Thermograms of DREADD and optogenetic experiments were collected at 0.5 Hz and 1 Hz, respectively and analysed with InfReC Analyzer NS9500 Professional software (Nippon Avionics). The highest temperature in one frame was used as the T_{BAT} of the mouse (Figs. 1b, 2c–e, 4b, c, Extended Data Figs. 4, 7d, e). These experiments were performed in a temperature-controlled chamber (HC-100, Shin Factory) at 22 °C.

For recordings of core body temperature, VO_2, EEG, electrocardiogram (ECG) and respiratory pattern, each animal was housed in a temperature-controlled chamber (HC-100, Shin Factory or LP-400P-AR, Nippon Medical & Chemical Instruments). To record the body temperature continuously, a telemetry temperature sensor (TA11TA-F10, DSI) was implanted in the animal's abdominal cavity under general inhalation anaesthesia at least seven days before recording. Artefacts on the recording of body temperature that were caused by animal movements were filtered by a custom R script based on a secondary trend model interpolation. VO_2 and the carbon dioxide output rate (VCO_2) of the animal were continuously recorded with a respiratory-gas analyser (ARCO-2000 mass spectrometer, ARCO system). The respiratory quotient was calculated as the ratio of VCO_2 to VO_2.

EEG and ECG were recorded by implanted telemetry transmitters (F20-EET or HD-X02, DSI). For EEG recording, two stainless-steel screws

(1-mm diameter) were soldered to the wires of telemetry transmitters and inserted through the skull of the cortex (AP, 1.00 mm; right, 1.50 mm from bregma or lambda) under general anaesthesia. Two other wires from the transmitter were placed on the surface of the thoracic cavity to record ECG. Animals were allowed at least 10 days to recover from surgery. The EEG and ECG data-collecting system consisted of transmitters, an analogue–digital converter and a recording computer with the software Ponemah Physiology Platform (v.6.30, DSI). The sampling rate was 500 Hz for both EEG and ECG, and data were converted to ASCII format for review. Heart rate was detected by QRS-complex peak-detection analysis of the EEG. Analysis of the heart-rate variability (HRV) was performed by resampling the train of R–R-interval (ms) into a 20-Hz time series followed by power-spectrum analysis by a 60-s window. The R–R-interval time series was detrended and a Hanning window was applied before frequency-domain analysis. High-frequency and low-frequency power (ms^2) were defined as the sum of 1.5–4 Hz and 0.4–1.5 Hz of the power spectrum of HRV, respectively[36].

Respiratory flow was recorded by a non-invasive respiratory flow recording system[37]. In brief, mice were placed in a metabolic chamber (TMC-1213-PMMA, Minamiderika Shokai), which had airflow of at least 0.3 l min^{-1}. The chamber was connected to a pressure sensor (PMD-8203-3G, Biotex), which detected the pressure difference between the outside and inside of the chamber. When the mouse is breathing, the pressure difference from outside to inside becomes larger during inspiration and smaller on expiration[37]. The analogue signal output from the sensor was digitized at 250 Hz by an AD converter (NI-9205, National Instruments) and stored on a computer by data-logging software developed by Biotex.

Metabolism recording during general anaesthesia

In addition to the body temperature, VO_2 and video recording described above (see 'Biological signal recordings'), the inlet of the metabolic chamber was directly connected to the outlet of the inhalation anaesthesia machine (NARCOBIT-E, Natsume Seisakusho). Animals were given 1% isoflurane at an ambient temperature of 28 °C for 30 min, followed by 90 min at an ambient temperature of 12 °C. After the experiment, the animals were warmed on a hot plate and recovery was confirmed.

Chemical analysis of blood

Blood was collected from anaesthetized mice by left ventricular puncture using a 25-gauge needle. The collected blood was stored on ice no longer than 2 h. Samples were centrifuged at 2,000*g* for 10 min at 4 °C, and supernatants were collected and frozen at −30 °C. Frozen serum samples were sent to Fujifilm Wako Pure Chemical Corporation to measure Na^+ (mM), K^+ (mM), Cl^- (mM), aspartate aminotransferase (IU l^{-1}), alanine transaminase (IU l^{-1}), lactic acid dehydrogenase (IU l^{-1}), creatine kinase (IU l^{-1}), glucose (mg dl^{-1}) and total serum ketone (μmol l^{-1}) levels.

Immunohistochemistry

Animals were deeply anaesthetized with isoflurane. They were perfused transcardially with 10% sucrose in water, followed by ice-cold 4% paraformaldehyde in 0.1 M phosphate buffer pH 7.4 (4% PFA), and the brain was removed. Brains were post-fixed overnight in 4% PFA at 4 °C, incubated overnight in 30% sucrose in 0.1 M phosphate buffered saline pH 7.4 (PBS) at 4 °C, immersed in Tissue-Tek OCT compound (Sakura) in cryomolds and frozen at −80 °C until sectioning. Brains were sliced coronally using a cryostat (CM1860, Leica) every 50 μm into four equal sets, collected in 6-well plates filled with ice-cold PBS and washed with PBS three times at room temperature. The following incubation steps were performed with mild shaking on an orbital shaker, unless stated otherwise. Brain sections were incubated in 1% Triton X-100 in PBS at room temperature for 1 h. The sections were blocked with 10% Blocking One (Nacalai Tesque) in 0.3% Triton X-100-treated PBS (blocking solution) for 1 h at room temperature without shaking. The sections were incubated in primary antibodies diluted with blocking solution (dilutions and types of each antibody are listed below) at 4 °C overnight, then washed three times, incubated with secondary antibodies at 4 °C overnight, washed with PBS, then mounted and coverslipped with HardSet Antifade Mounting Medium with DAPI (Vectashield).

The primary antibodies used in this study were; rabbit anti-cFOS (1:4,000, ABE457, Millipore), goat anti-mCherry (1:15,000, AB0040-200, Sicgen), rat anti-GFP (1:5,000, 04404-84, Nacalai Tesque), mouse anti-TH (1:1,000, sc-25269, Santa Cruz Biotechnology), mouse anti-orexin-A (1:200, sc-80263, Santa Cruz Biotechnology) and rabbit anti-MCH (1:2,000, M8440, Sigma). The secondary antibodies were: Alexa Fluor 488 donkey anti-rat, 488 donkey anti-rabbit, 594 donkey anti-rabbit, 594 donkey anti-goat, 647 donkey anti-mouse and 647 donkey anti-rabbit (1:1,000, Invitrogen). For Nissl staining, sections were counterstained with NeuroTrace 435/455 blue fluorescent Nissl stain (1:500, N-21479, Invitrogen) during the secondary antibody step, and coverslipped with FluorSave Reagent (Millipore). Brain sections were observed using an Axio Zoom.V16 (Zeiss) and a TCS SP8 laser confocal microscope (Leica). Brain regions were defined according to the brain maps adapted from Paxinos and Franklin's atlas of the mouse brain[38] and Paxinos and Watson's atlas of the rat brain[39]. Some maps in these books were modified to simply depict stereotaxic orientation.

In situ hybridization

Fluorescence in situ hybridization was performed with the RNAscope Fluorescent Multiplex Kit (Advanced Cell Diagnostics) using the following probes: Probe-Mm-*Qrfp* 464341, *mCherry* 431201-C2, Mm-*Slc32a1* 319191-C3, Mm-*Slc17a6* 319171, Mm-*Adcyap1* 405911-C2, Mm-*Bdnf*-CDS 457761-C3, Mm-*Ptger3*-O1 501831-C3 and Rn-*Qrfp* 834441.

Mice or rats were perfused and fixed in fresh 4% PFA and brains were processed until sectioning by the same method as described in 'Immunohistochemistry' except using DEPC-treated PBS. Brains were sectioned coronally into six sections (20 μm) with a cryostat (Leica), and mounted on Superfrost Plus microscope slides (Fisherbrand). Pretreatment procedures (post-fixation and dehydration) and RNAscope fluorescent multiplex assay were performed following the RNAscope Assay Guide (document numbers 320513 and 320293). For the combination with immunohistochemistry, after the amplification phase, samples were immediately moved into the washing phase of immunohistochemistry using slide vats. Then, the slides were processed with the same procedure as was used for immunohistochemistry.

Cell counting

Images of FOS experiments (Fig. 1c) and fluorescence in situ hybridization (Fig. 4a, Extended Data Figs. 11d, 12f) were obtained with a TCS SP8 laser confocal microscope (Leica), and *z*-stacked to 25 μm and 10 μm, respectively. Images were counted using image-analysing software (LAS X, Leica). In Fig. 1c, mCherry-expressing Q neurons and FOS signals were quantified by counting 6 sections from mice ($n = 3$) per group (0.50 and 0.26 mm from bregma). In Fig. 4a, Q neurons, *Vglut2*- and *Vgat*-expressing cells were quantified by counting 6 sequential sections from Q-hM3D mice ($n = 2$ slices of 0.50, 0.38 and 0.26 mm from bregma as shown in the figure). In Extended Data Fig. 11d, Q neurons, *Adcyap1*-, *Bdnf*- and *Ptger3*-expressing cells were calculated by counting 6 sections from Q-hM3D mice ($n = 2$; same series of slices as Fig. 4a).

Retrograde tracing

Male $Qrfp^{iCre}$ mice (10–12 weeks old) were injected with viruses as shown below. First, 0.16 μl AAV_{10}-DIO-TVA-mCherry and 0.33 μl AAV_{10}-DIO-RG were delivered to express TVA–mCherry and rabies glycoprotein (RG) in Q neurons in the AVPe/MPA (AP, 0.38 mm; ML, 0.25 mm; DV, −5.25 mm from bregma) unilaterally. Three weeks later, 0.3 μl SADΔG-GFP(EnvA) was injected at the same site. Six days later, mice were fixed and treated according to the immunohistochemistry procedure. Whole

brain sections were observed to detect starter (mCherry and GFP double-positive) neurons and input (GFP-positive) neurons using an Axio Zoom.V16 (Zeiss) and a TCS SP8 laser confocal microscope (Leica).

Optogenetic manipulation

Mice were connected with optical fibre patch cable (200-μm diameter; NA: 0.22, 1.0 m long; Doric Lenses). We used DPSS lasers (473-nm blue or 589-nm yellow; Shanghai Laser) to apply optogenetic manipulations. The laser power at the optic fibre tip was adjusted to 8–10 mW. In Fig. 2c–e, 473-nm laser stimulation was applied at 1 Hz for 1 s every 30 min (repeated 4 times), controlled by a TTL pulse generator (Amuza). In Extended Data Fig. 7e, a 473-nm laser was applied at 1 Hz for 1 s every 60 min (repeated 3 times) and a 589-nm laser was applied at 1 Hz for 5 s 3 min after the second stimulation with the 473-nm laser. Mice with incorrect fibre placement were excluded from data analysis.

Behavioural tests

All behavioural tests were performed during the dark phase, with five Q-hM3D mice and five *Qrfp*^{iCre} mice that were injected with AAV$_{10}$-DIO-mCherry into the AVPe/MPA. After AAV injection, mice were housed singly in home cages and allowed to recover for two weeks, then acclimated to the experimenter's handling. All tests except the rotarod test were recorded with a visual video camera (FDR-AX60, Sony) and analysed by Smart Video Tracking Software (Panlab, Harvard Apparatus). We performed behavioural tests in the following order, one test each day.

Open-field tests were performed by using a square open-field arena (made of opaque plastic, W40 × D40 × H30 cm) with dim light (less than10 lx). Each mouse was placed in and allowed to freely explore the arena for 20 min. The arena was wiped with 70% ethanol and weakly acidic water after each session.

Novel object recognition tests were carried out in the same arena as the open-field tests. The mice were put in the centre of the arena, allowed to explore for 20 min and to touch two identical objects (object A) placed symmetrically. One day later, the mice were put back in the arena for the novel object recognition test trial. For the test trials, one of the previous familiar objects (object A) remained in the arena, but the other one was replaced with a novel object (object B). The time spent in the area of each object (a 5-cm-diameter circle with the object at the centre) was measured for calculating a discrimination ratio defined as follows: (Time B − Time A)/(Time A + Time B). The objects were a 25-ml cell culture flask filled with sand; and stacked plastic blocks. Flasks and blocks were randomly assigned as object A or B in each experiment.

Elevated plus maze tests were conducted on an apparatus made of white plastic, consisting of a central area (5 × 5 cm), two open arms (25 × 5 cm) and two closed arms (25 × 5 cm) with 25-cm high walls with 10 lx illumination. The mouse was put in the central area and allowed to explore for 15 min.

Rotarod tests were performed using an accelerating rotarod (Ugo Basile) in which a mouse was placed on the rotating drum (3-cm diameter). The initial speed of the rotarod was set at 4 rpm. The speed gradually increased from 4 to 40 rpm over 300 s.

For tail suspension tests, mice were suspended from their tails by a strip of masking tape that was placed approximately 2 cm from the tip of the tail for 5 min.

A week after behavioural tests, all mice were fixed, and haematoxylin and eosin staining was performed using the standard method.

Measuring daily body weight, food intake and locomotor activity

We measured daily body weight, food intake and locomotor activity before and after QIH induction in six Q-hM3D mice. Body weight and amount of chow consumed were measured at the beginning of the dark period. On days 4 and 6, saline and CNO (1 mg kg^{-1}) were administrated intraperitoneally at a volume of 10 μl g^{-1}, respectively. Locomotor activity was constantly detected throughout all experimental days with a customized device for sensing object locomotion, which was placed 25 cm above the home cage and enclosed in a sound attenuating chamber (Muromachi). The data were analysed with SOF-860 software (Med Associates) and retrieved every hour.

Electrophysiological analysis

Mice were decapitated under deep anaesthesia with isoflurane (Pfizer). Brains were extracted and cooled in ice-cold cutting solution containing the following: 125 mM choline chloride, 25 mM $NaHCO_3$, 10 mM D(+)-glucose, 7 mM $MgCl_2$, 2.5 mM KCl, 1.25 mM NaH_2PO_4 and 0.5 mM $CaCl_2$ bubbled with O_2 (95%) and CO_2 (5%). Horizontal brain slices (250-μm thickness), including the hypothalamus, were prepared with a vibratome (VT1200S, Leica) and maintained for 1 h at room temperature in artificial cerebrospinal fluid (ACSF) containing the following: 125 mM NaCl, 26 mM $NaHCO_3$, 10 mM D(+)-glucose, 2.5 mM KCl, 2 mM $CaCl_2$ and 1 mM $MgSO_4$ bubbled with O_2 (95%) and CO_2 (5%). The electrodes (5–8 MΩ) were filled with an internal solution containing the following: 125 mM K-gluconate, 10 mM HEPES, 10 mM phosphocreatine, 0.05 mM tolbutamide, 4 mM NaCl, 4 mM ATP, 2 mM $MgCl_2$, 0.4 mM GTP and 0.2 mM EGTA, pH 7.3, adjusted with KOH). Firing of hM3Dq-mCherry-expressing neurons was recorded in the current-clamp mode at a temperature of 30 °C. CNO (1 μM) was bath-applied to examine the effects. The combination of a MultiClamp 700B amplifier, Digidata 1440A A/D converter and Clampex 10.3 software (Molecular Devices) was used to control membrane voltage and data acquisition.

Induction of FIT

Each FIT-induction experiment was designed to record the metabolism of the mouse for at least three days. The mice were introduced to the chamber the day before recording started (day 0). Food and water were freely available. The ambient temperature was set as indicated on day 0 and kept constant throughout the experiment. A telemetry temperature sensor implanted in the mouse was turned on before placing it in the chamber. The standard experimental design was as follows: on day 2, zeitgeber time (ZT) 0, food was removed to induce torpor. After 24 h, on day 3, at ZT0, food was returned to each animal.

Three-dimensional imaging of transparent mouse brain

Transparent mouse brains were generated by the Sca*l*eS method as described previously[40]. ScaleS solutions were made using urea crystals (Wako Pure Chemical Industries, 217-00615), D(−)-sorbitol (Wako Pure Chemical Industries, 199-14731), methyl-β-cyclodextrin (Tokyo Chemical Industry, M1356), γ-cyclodextrin (Wako Pure Chemical Industries, 037-10643), *N*-acetyl-L-hydroxyproline (Skin Essential Actives, Taiwan), dimethyl sulfoxide (DMSO) (Wako Pure Chemical Industries, 043-07216), glycerol (Sigma, G9012) and Triton X-100 (Nacalai Tesque, 35501-15). Brains of *Qrfp*^{iCre} mice injected with AAV$_9$-hSYN-DIO-GCaMP6 s were fixed and cleared with ScaleS. Images were obtained with a laser confocal microscope (Olympus, FV1200 with XLSLPN25XGMP (NA 1.00, WD: 8 mm) (RI: 1.41–1.52)).

Statistical analysis

In this study, we used Bayesian statistics to evaluate our hypothesis and experimental results. We designed a statistical model with parameters representing the structure of the hypothesis and fitted the model to the experimental results. Bayesian inference estimates the posterior probability distribution of the model parameters from the likelihood distribution and prior probability distribution of the parameters. The posterior distributions provide information on how the model can describe the hypothesis from the experimental results. Bayesian modelling can explicitly include all types of uncertainty; therefore, it can deal with data with noise in the observation or it can fully use information from a small number of samples that potentially have a wide range of uncertainty. Furthermore, it can deal with multiple layers of multiple groups with different numbers of samples using hierarchical models.

All of these advantages of Bayesian inference render it an appropriate method for handling commonly seen issues in animal experiments. Model fitting was performed using Hamiltonian Monte Carlo with its adaptive variant, the No-U-turn Sampler, as implemented in Stan v.2.18.0 with the RStan library[41] in R v.3.52[42]. We assessed convergence by inspection of the trace plots, Gelman and Rubin's convergence diagnostic and an estimate of the effective number of samples. The model priors were defined to be weakly informative and conservative, which are specified in the following sections. The fundamental principles and techniques for designing the statistical models were based on a previous publication[43]. The source code for the models and the data used for analysis are available at https://briefcase.riken.jp/public/JjtgwAnqQ8lAgyI.

Body weights of $Qrfp^{iCre}$ mice were modelled at a given age and strain by a state-space hierarchical model (Extended Data Fig. 1d, e, code folder QRFP_KO_BW). Mice in each group (wild-type mice ($n = 9$), heterozygous ($n = 9$) and homozygous ($n = 10$) $Qrfp^{iCre}$ mice) were raised in each cage without identification of individuals. When the unobservable baseline of body weight is defined as a time-variable $B_{t,s}$, in which t is the time point and s is the index of strains (1, 2 and 3 for wild-type, heterozygous and homozygous $Qrfp^{iCre}$ mice, respectively), with the trend $\eta_{t,s}$ and the total time point T, the observed state $Y_{t,i}$ can be described by modelling the observational error by a log-normal distribution as:

$$Y_{t,s} \approx \text{log-normal}\left[\log(B_{t,s}) - \frac{(\sigma_1)^2}{2},\ \sigma_1\right] \tag{1}$$

$$\begin{cases} B_{1,s} = +\eta_1,\ t = 1 \\ B_{2,s} - B_{1,s} = B_{1,s} + \eta_{2,s},\ t = 2 \\ B_{t,s} - B_{t-1,s} = B_{t-1,s} - B_{t-2,s} + \eta_{t,s},\ t \geq 3 \end{cases} \tag{2}$$

$$\eta_{t,s} \approx \text{Normal}(0, \sigma_2) \tag{3}$$

$$t = 1 \cdots T \tag{4}$$

$$s = \{1,\ 2,\ 3\} \tag{5}$$

Uniform priors were applied for every parameter except σ_1 and σ_2, which were drawn from standard half-normal distribution.

The spiking frequency of *Qrfp*-positive neurons in brain slices was modelled by parameterizing the difference in spiking frequency when neurons were activated by CNO (Extended Data Fig. 3c–e, code folder Patch_M3_CNO). When the total number of slices is K, and the observed spiking frequencies of the control and CNO-administered recording of the ith slice are B_i and C_i, respectively, B_i is modelled by β_{BASE} with observational errors, and C_i is modelled by the sum of β_{BASE} and β_{CNO} with observational errors. Because spiking frequency is a positive real number, errors can be modelled by a log-normal distribution; therefore, B_i and C_i can be described as:

$$B_i \approx \text{log-normal}\left(\log(\beta_{BASE}) - \frac{(\sigma_{ERROR})^2}{2},\ \sigma_{ERROR}\right) \tag{6}$$

$$C_i \approx \text{log-normal}\left(\log(\beta_{BASE} + \beta_{CNO}) - \frac{(\sigma_{ERROR})^2}{2},\ \sigma_{ERROR}\right) \tag{7}$$

$$\beta_{BASE} \approx \text{Normal}(0,\ \sigma_{BASE}) \tag{8}$$

$$\beta_{CNO} \approx \text{Normal}(0,\ \sigma_{CNO}) \tag{9}$$

$$i = 1 \cdots K \tag{10}$$

All σ values were sampled from standard half-normal distributions.

T_{BAT} values of optogenetically or chemogenetically stimulated mice were modelled in a hierarchical multilevel model (Figs. 2d, 4c; code folders TBAT_Opt and TBAT_Flox). Four groups of mice were included in this experiment. T_{BAT} was recorded at 1 Hz, and every 10 s the 10-s maximum was stored for further analysis. Ten-minute recording of every T_{BAT} of interest was included in the analysis. When K is the total number of mice, and Y is T_{BAT} during the duration of interest of mouse j that belongs to group i, Y can be described as the sum of the global mean parameter β, the group parameter β_{GROUP} and the individual mouse parameter β_{MOUSE} with the observational noise modelled in a Cauchy distribution of a scale parameter σ_{ERROR} as:\

$$Y_{i,j} \approx \text{Cauchy}\left(\beta + \beta_{GROUP[i]} + \beta_{MOUSE[j]},\ \sigma_{ERROR}\right) \tag{11}$$

$$\beta_{GROUP} \approx \text{Normal}(0,\ \sigma_{GROUP}) \tag{12}$$

$$\beta_{MOUSE} \approx \text{Normal}(0,\ \sigma_{MOUSE}) \tag{13}$$

$$i = \{1,\ 2,\ 3,\ 4\} \tag{14}$$

$$j = 1 \cdots K \tag{15}$$

All σ values were sampled from standard half-normal distributions. Differences in T_{BAT} among groups were compared by estimating the mean T_{BAT} for each group from posterior distributions, which is the sum of β and β_{GROUP} with normally distributed noise at a standard deviation of σ_{MOUSE}.

To evaluate the thermoregulatory system during QIH and normal conditions, heat loss and production of the animal was described in a hierarchical multilevel model (Fig. 3c–k, code folder QIH_GTRH). Three parameters (G, T_R and H) during two metabolic conditions (normal and QIH) were estimated from the metabolically stable state of the animal at various ambient temperatures. The detailed methods have previously been described[5]. In brief, a linear model consisting of the controllable parameter T_A and the observable parameters T_B and VO_2 was fitted to the experimental results for both T_B and VO_2 using T_A as a predictor with normally distributed noise. The posterior distribution of the slope and intercept coefficients for each model were then used to estimate G, T_R and H. For estimation of T_R and H, the model is designed for monotonically increasing T_B and decreasing VO_2 against T_A. Therefore, the parameter estimation during QIH used T_B and VO_2 during T_A = 16 °C, 20 °C and 24 °C (Fig. 3b, Extended Data Fig. 8b). In this analysis, priors of the standard deviation of the noise were standard half-normal distributions, and the other parameters used the positive region of uniform distribution except the intercept coefficient of T_B, which used uniform distribution owing to possible negative values.

The circadian transition of metabolism in Q-TeTxLC mice was analysed by modelling the metabolism by clustering the recorded values into the light phase (L-phase) and the dark phase (D-phase) (Extended Data Fig. 10h, code folder TeTxLC_LD). Specifically, when Y is the observed T_B of group i at phase j, Y can be described as the sum of base metabolism (light-phase metabolism) and the difference between the dark phase with normally distributed observational noise as:

$$Y_{i,\ j} \approx \text{Normal}\left(\beta_{BASE[i]} + \beta_{DARK[i]} P_j,\ \sigma_{ERROR}\right) \tag{16}$$

$$\beta_{BASE} \approx \text{Normal}(0,\ \sigma_{BASE}) \tag{17}$$

$$\beta_{\mathrm{DARK}} \approx \mathrm{Normal}(0, \sigma_{\mathrm{DARK}}) \quad (18)$$

$$i = \{1\text{: control},\ 2\text{: TeTxLC}\} \quad (19)$$

$$j = \{1\text{: L-phase},\ 2\text{: D-phase}\} \quad (20)$$

$$\begin{cases} P_1 = 0 \\ P_2 = 1 \end{cases} \quad (21)$$

All σ values were sampled from standard half-normal distributions. For modelling VO_2, the fundamental model structure was identical to T_B modelling except that the observational error was modelled as a log-normal distribution because VO_2 assumes only positive real numbers.

Statistics and reproducibility

The number of animals or samples used in each experiment are stated in the manuscript or in the figures. The numbers of experimental repetitions were as follows: Fig. 1a, 4 times (coronal) and 3 times (horizontal); Fig. 1b, 12 times; Fig. 1c, 3 times; Fig. 2a, b, 3 times; Fig. 2e, 6 times; Fig. 3a: numbers of mice are: 6, 11, 5, 5, 6, 6 and 6 for T_A = 8, 12, 16, 20, 24, 28 and 32 °C, respectively; Fig. 3l, 4 times; Fig. 4a, 3 times; Extended Data Fig. 1b, c, 3 times; Extended Data Fig. 2b, twice (horizontal) and 3 times (coronal); Extended Data Fig. 3, twice (a) and 9 times (b); Extended Data Fig. 4, twice; Extended Data Fig. 5b, 5 times; Extended Data Fig. 6e, twice; Extended Data Fig. 6f, 4 times; Extended Data Fig. 7b–d, 3 times; Extended Data Fig. 10, once (b) and 3 times (c); Extended Data Fig. 11, 3 times (b, c) and twice (d, e); Extended Data Fig. 12, 4 times (c) and twice (e, f); Supplementary Video 2, twice; Supplementary Video 3, 6 times; and Supplementary Video 4, 4 times.

Reporting summary

Further information on research design is available in the Nature Research Reporting Summary linked to this paper.

Data availability

Data used for Bayesian estimation are included with the source code. Other data are available from the corresponding authors on request.

Code availability

All of the source code of the models used for Bayesian estimation is available at https://briefcase.riken.jp/public/JjtgwAnqQ8lAgyI. See 'Statistical analysis' in Methods for details.

33. Mieda, M. et al. Cellular clocks in AVP neurons of the SCN are critical for interneuronal coupling regulating circadian behavior rhythm. *Neuron* **85**, 1103–1116 (2015).
34. Osakada, F. & Callaway, E. M. Design and generation of recombinant rabies virus vectors. *Nat. Protoc.* **8**, 1583–1601 (2013).
35. Saito, Y. C. et al. Monoamines inhibit GABAergic neurons in ventrolateral preoptic area that make direct synaptic connections to hypothalamic arousal neurons. *J. Neurosci.* **38**, 6366–6378 (2018).
36. Gehrmann, J. et al. Phenotypic screening for heart rate variability in the mouse. *Am. J. Physiol. Heart Circ. Physiol.* **279**, H733–H740 (2000).
37. Sunagawa, G. A. et al. Mammalian reverse genetics without crossing reveals *Nr3a* as a short-sleeper gene. *Cell Rep.* **14**, 662–677 (2016).
38. Franklin, K. B. J. & Paxinos, G. *The Mouse Brain in Stereotaxic Coordinates* 3rd edn (Academic Press, 2007).
39. Paxinos, G. & Watson, C. *The Rat Brain in Stereotaxic Coordinates* 7th edn (Academic Press, 2013).
40. Hama, H. et al. Sca*l*eS: an optical clearing palette for biological imaging. *Nat. Neurosci.* **18**, 1518–1529 (2015).
41. Stan Development Team. RStan: the R interface to Stan. R package v.2.19.3 (2020).
42. R Core Team. R: A language and environment for statistical computing, v.2.18.0 (R Foundation for Statistical Computing, 2018).
43. McElreath, R. *Statistical Rethinking: a Bayesian Course with Examples in R and Stan* 1st edn (CRC Press, 2016).
44. Romanov, R. A. et al. Molecular interrogation of hypothalamic organization reveals distinct dopamine neuronal subtypes. *Nat. Neurosci.* **20**, 176–188 (2017).
45. Wickersham, I. R. et al. Monosynaptic restriction of transsynaptic tracing from single, genetically targeted neurons. *Neuron* **53**, 639–647 (2007).
46. Wang, T. A. et al. Thermoregulation via temperature-dependent PGD_2 production in mouse preoptic area. *Neuron* **103**, 309–322 (2019).
47. Tan, C. L. & Knight, Z. A. Regulation of body temperature by the nervous system. *Neuron* **98**, 31–48 (2018).
48. Lazarus, M. et al. EP3 prostaglandin receptors in the median preoptic nucleus are critical for fever responses. *Nat. Neurosci.* **10**, 1131–1133 (2007).

Acknowledgements This study was supported by a JSPS KAKENHI Grant-in-Aid for Scientific Research (B) (JP 18H02595) (T.S.); a JSPS KAKENHI Grant-in-Aid for Scientific Research on Innovative Areas 'Willdynamics' (16H06401); JSPS KAKENHI grant number JP19K22465 (T.S.); JST CREST grant number JPMJCR1655 Japan (T.S.); the RIKEN Special Postdoctoral Researcher program (G.A.S.); a JSPS KAKENHI Grant-in-Aid for Scientific Research on Innovative Areas 'Thermal Biology' (18H04706) (G.A.S.); a JSPS KAKENHI Grant-in-Aid for Scientific Research (A) (19H01066) (G.A.S.); a research grant from the Astellas Foundation for Research on Metabolic Disorders (G.A.S.); and JSPS KAKENHI grant number 19J20876 (T.M.T.). We thank the animal resource centre at the University of Tsukuba and LARGE, RIKEN BDR for housing the mice; Y. Cherasse for preparing virus vectors; A. Miyasaka and Y. Niwa for discussion; and W. Gray for proofreading the manuscript. All of the brain diagrams used in figures were made based on the illustrations in Paxinos and Franklin's atlas of the mouse brain[38] and Paxinos and Watson's atlas of the rat brain[39].

Author contributions T.M.T., G.A.S. and T.S. conceived the project and designed the experiments. T.M.T. performed all stereotaxic surgeries and tissue samplings and conducted experiments except as noted. T.M.T., K.I., M.T. and G.A.S. performed metabolism and biological signal-recording experiments. T.M.T. and S.S. performed histology analyses. M.A., M.Y., T.S. and K. Sakimura designed and generated genetically modified mice. T.S. and K. Sakurai. prepared AAV vectors. T.S. prepared rabies virus vectors. H.H. and A.M. performed three-dimensional imaging of transparent brains. E.H. performed electrophysiology experiments. G.A.S. performed the statistical analyses. T.M.T., G.A.S. and T.S. wrote the manuscript, with input from all co-authors.

Competing interests The authors declare no competing interests.

Additional information

Supplementary information is available for this paper at https://doi.org/10.1038/s41586-020-2163-6.

Correspondence and requests for materials should be addressed to G.A.S. or T.S.

Peer review information *Nature* thanks Rob Henning, Shaun Morrison, Richard Palmiter and the other, anonymous, reviewer(s) for their contribution to the peer review of this work.

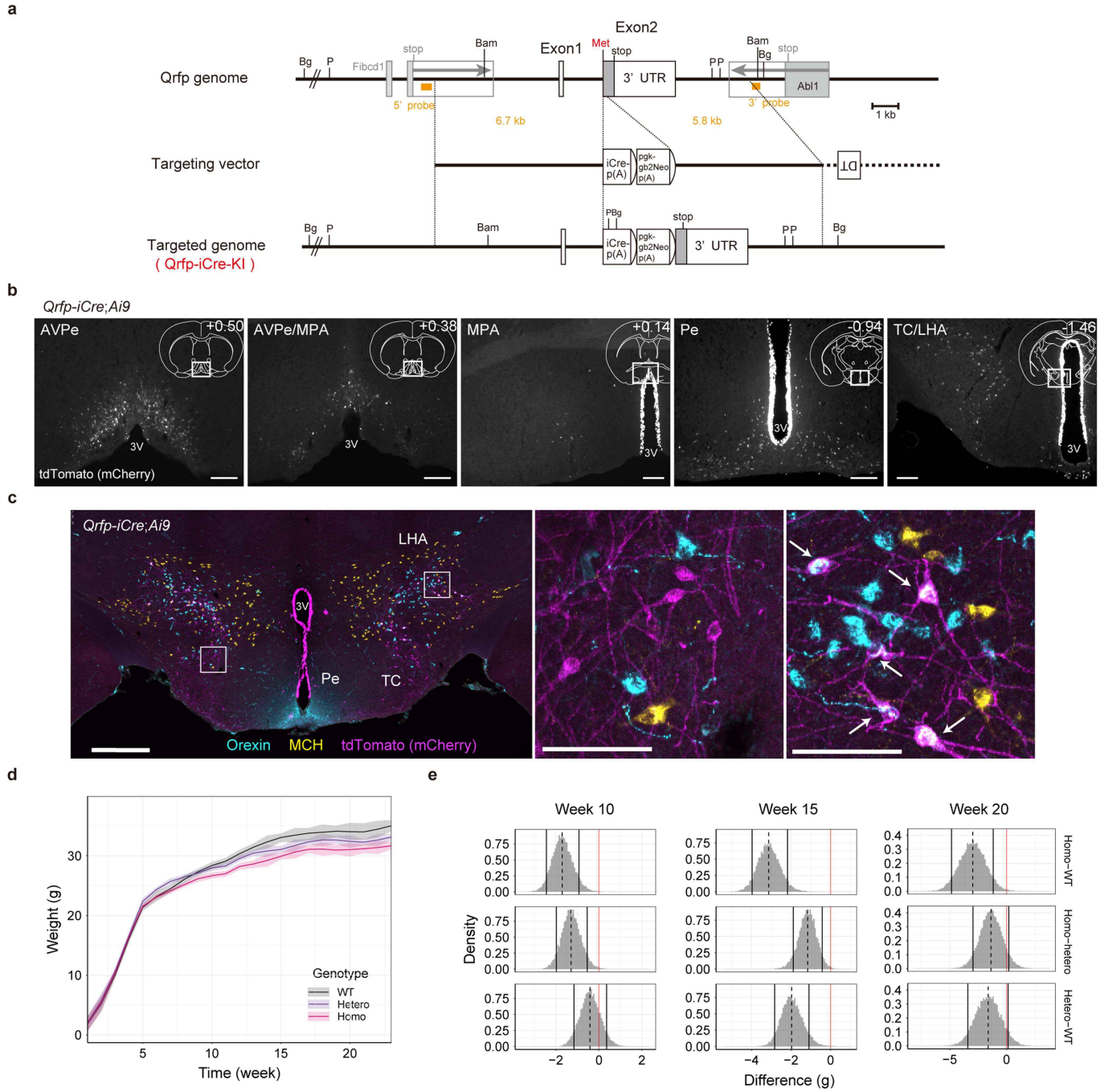

Extended Data Fig. 1 | Generation of *Qrfp*^{iCre} mice. To examine the role of QRFP-producing neurons, we engineered mice in which codon-improved Cre recombinase (*iCre*) is inserted in the *Qrfp* allele. **a**, Targeting vector and structure of the targeted allele of *Qrfp*^{iCre} mice. We mated mice with the targeted genome with FLP66 mice to delete the pgk-Neo cassette and create the *Qrfp*^{iCre} mice used in this study. **b**, Distribution of Cre-positive neurons in coronal sections of brain prepared from *Qrfp*^{iCre}*;Ai9* mice. Scale bars, 200 µm. **c**, Immunostaining of hypothalamic slices prepared from a *Qrfp*^{iCre}*;Ai9* mouse with anti-mCherry, anti-orexin and anti-melanin-concentrating hormone (MCH) antibodies. Along the wall of the third ventricle, we found extensive expression of mCherry, presumably derived from tanycytes and ependymal cells. However, we could not express exogenous genes by injecting Cre-dependent AAV vectors into this region in adult mice, suggesting transient expression of Cre in these cells during the developmental stage. In addition, we observed the existence of iCre-positive neurons in the LHA in reporter mice crossed with *Qrfp*^{iCre} mice that were also positive for orexin-like immunoreactivity—although a previous study did not find orexin and QRFP double-positive cells in adult mice[13]. This suggests that a low level of iCre is expressed in some orexin neurons, and that orexin neurons and QRFP neurons might be derived from the same cell lineage. Single-cell RNA-sequencing analysis of the hypothalamus showed colocalization of *Qrfp* and *Orexin* (also known as *Hcrt*), and hierarchical clustering defined by molecular fingerprints showed that orexin- and QRFP-expressing neurons have a close neuronal lineage[44]. The middle and right images are magnifications of the boxed areas. QRFP-expressing neurons in the LHA were positive for mCherry (arrows) but negative for MCH. Scale bars, 500 µm (left); 100 µm (middle, right). **d**, Growth curve of *Qrfp*^{iCre} mice ($n = 9$ wild type (WT), $n = 9$ *Qrfp*^{iCre} heterozygous and $n = 10$ *Qrfp*^{iCre} homozygous). Lines show median and shaded areas denote the estimated 89% HPDI of the body weight of each group at a given age. **e**, Posterior distribution of estimated difference in body weight between two groups. The dotted line shows median and solid lines denote 89% HPDI of differences. Homozygous *Qrfp*^{iCre} mice are smaller than wild-type mice, consistent with a previous observation[13].

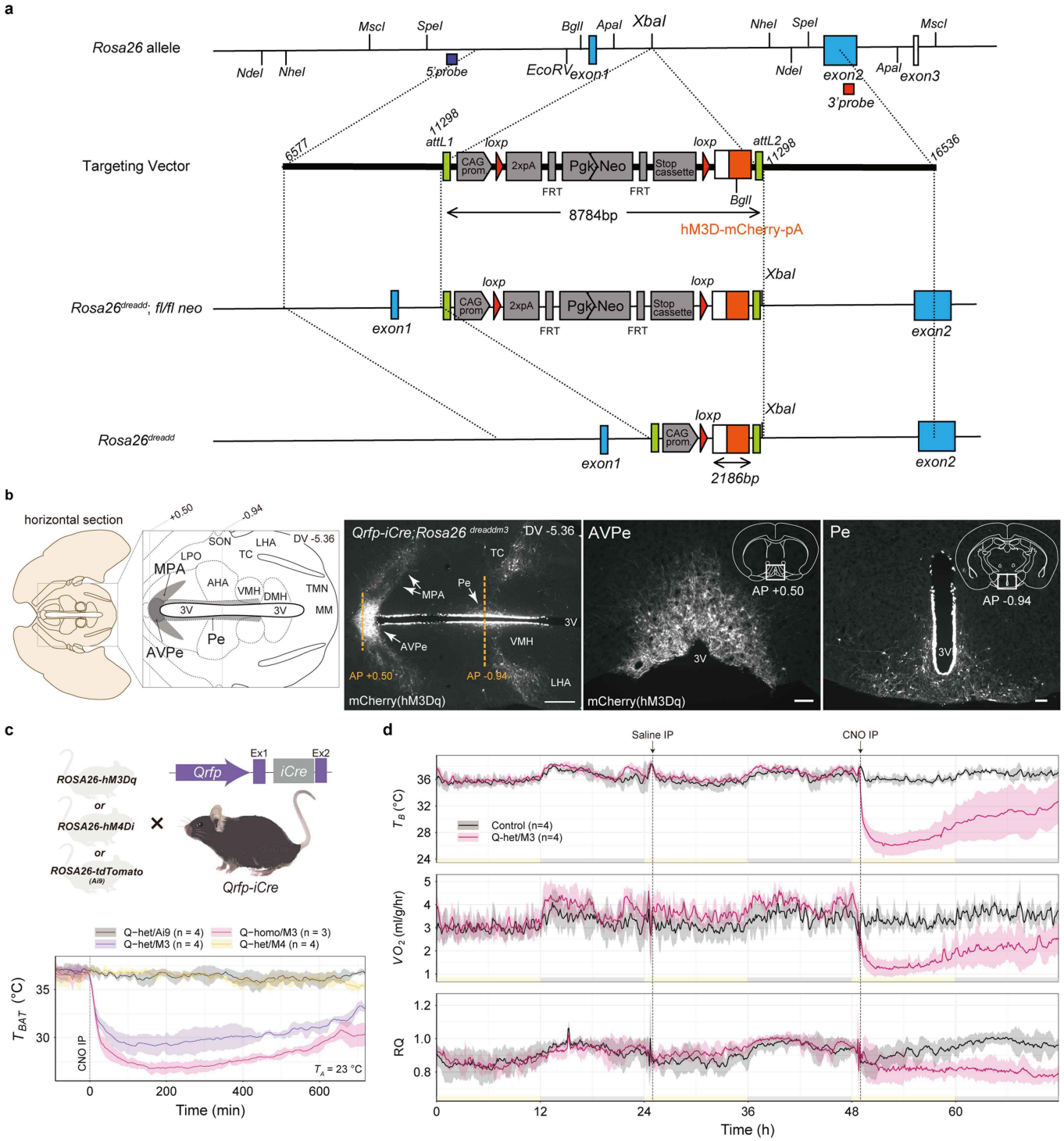

Extended Data Fig. 2 | See next page for caption.

Extended Data Fig. 2 | Expression of DREADD receptors in *Qrfp*^{iCre} neurons. We generated *Rosa26*^{dreaddm3} mice and crossed them with *Qrfp*^{iCre} mice (Extended Data Fig. 1) to obtain mice that express hM3Dq-mCherry exclusively in iCre-expressing cells (*Qrfp*^{iCre};*Rosa26*^{dreaddm3} mice). **a**, Generation of mice that express hM3Dq and hM4Di in Cre-expressing neurons. Targeting vectors and structures of the targeted alleles of *Rosa26*^{dreaddm3} and *Rosa26*^{dreaddm4} mice. We mated these mice with FLP66 mice to delete the pgk-Neo cassette. Orange boxes indicate hM3Dq-mCherry or hM4Di-mCherry. Because the CAG promoter drives expression of hM3Dq-mCherry or hM4Dq-mCherry only after Cre-mediated excision of the floxed stopper element, this allowed us to express hM3Dq or hM4Di specifically in Cre-expressing neurons. **b**, Horizontal and coronal sections of brain prepared from a *Qrfp*^{iCre};*Rosa26*^{dreaddm3} mouse, showing the distribution of mCherry-positive neurons in the hypothalamus. **c**, Top, strategy for chemogenetic excitation or inhibition of whole iCre-positive neuronal populations in *Qrfp*^{iCre} mice. Bottom, chemogenetic excitation of iCre-positive cells in *Qrfp*^{iCre} mice induced hypothermia. Heterozygous (Q-het) or homozygous (Q-homo) *Qrfp*^{iCre} mice with heterozygous *Rosa26*^{dreaddm3} (M3) and/or *Rosa26*^{dreaddm4} (M4) alleles were subjected to experiments. CNO was administered at ZT12 (start of the dark period). The ambient temperature was 23 °C. We found that excitatory manipulation of *Qrfp*^{iCre} neurons in mice resulted in severe immobility. As the posture of these mice was similar to that observed during daily torpor, we initially postulated that activation of iCre-positive cells induced a daily torpor-like state. To evaluate this hypothesis, we measured body temperature and found that the induced state of immobility was accompanied by marked, long-lasting hypothermia. T_{BAT} decreased beginning about 5 min after CNO administration and lasted 12 h. Mice spontaneously recovered without external warming. By contrast, inhibitory DREADD manipulation of iCre-positive neurons did not have any effect on T_{BAT}. Notably, hM3Dq-mediated activation of iCre-positive neurons in *Qrfp*^{iCre};*Rosa26*^{dreaddm3} mice induced robust hypothermia, even in homozygous *Qrfp*^{iCre} mice in which *Qrfp* sequences are completely replaced by *iCre* in both alleles. This suggests that QRFP itself does not have a role in inducing hypothermia. The degree of hypothermia was greater in QRFP-deficient mice, which indicates that endogenous QRFP itself counteracts the hypothermia. **d**, Excitatory manipulation of Q neurons in *Qrfp*^{iCre};*Rosa26*^{dreaddm3} mice in the light period (at ZT1) also induced a long-lasting hypothermic state ($n = 4$ mice for each condition). Line and shading in **c**, **d** denote mean and s.d. of each group. AHA, anterior hypothalamus; ARC, arcuate nucleus; LPO, lateral preoptic area; MM, medial mammillary nucleus; SON, supraoptic nucleus; TMN, tuberomammillary nucleus; VMH, ventromedial hypothalamus.

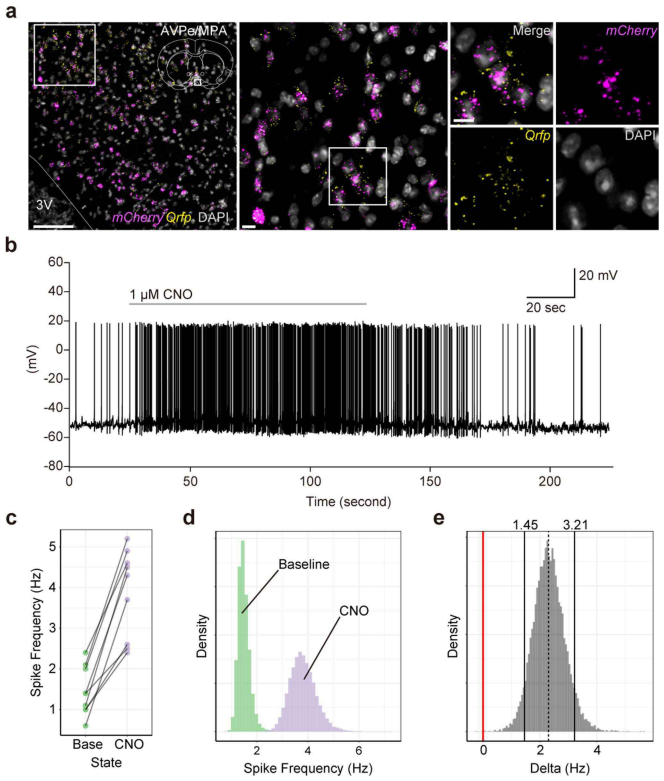

Extended Data Fig. 3 | DREADD-mediated excitation of Q neurons. a, *Qrfp* mRNA is expressed in mCherry-positive neurons in Q-hM3D mice. Dual-colour in situ hybridization for *Qrfp* and *mCherry* mRNA in brain slices prepared from Q-hM3D mice. We confirmed that CNO administration induced QIH, and subjected the mice to histological analysis. All mCherry-positive neurons were positive for *Qrfp* expression. Scale bars, 100 μm (left); 10 μm (middle, right). **b**, Representative trace of current-clamp recording from mCherry-positive Q neurons in a slice prepared from Q-hM3D mice. We performed the experiments nine times and obtained the same results. **c**, Comparison of spike frequency at baseline and after treatment with CNO ($n = 9$). **d**, Estimated distribution of spike frequency in baseline and CNO-treated slices. **e**, The estimated difference in spike frequency between CNO-treated and baseline slices was [1.44, 2.80] Hz. Because the 89% HPDI of the estimated difference is positive, the spike frequency in CNO-treated slices may be larger than baseline by more than 89%.

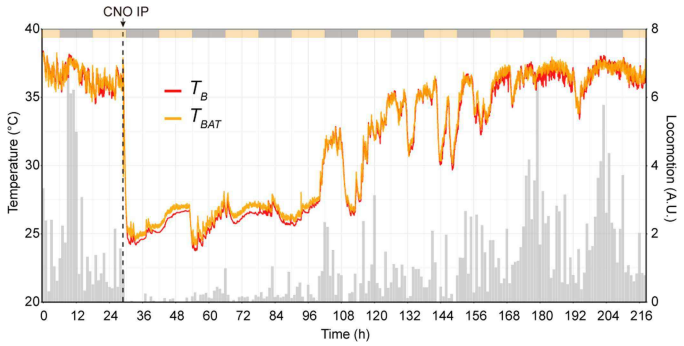

Extended Data Fig. 4 | T_{BAT} decreases concomitantly with body temperature during QIH. Representative traces of T_{BAT} examined by thermographic camera (orange) and body temperature measured by telemetry sensor (red) before and after induction of QIH in a Q-hM3D mouse, simultaneously. Grey bars indicate locomotor activity. Note that T_{BAT} and body temperature show almost the same values both before and after induction of QIH. A.U. arbitrary units.

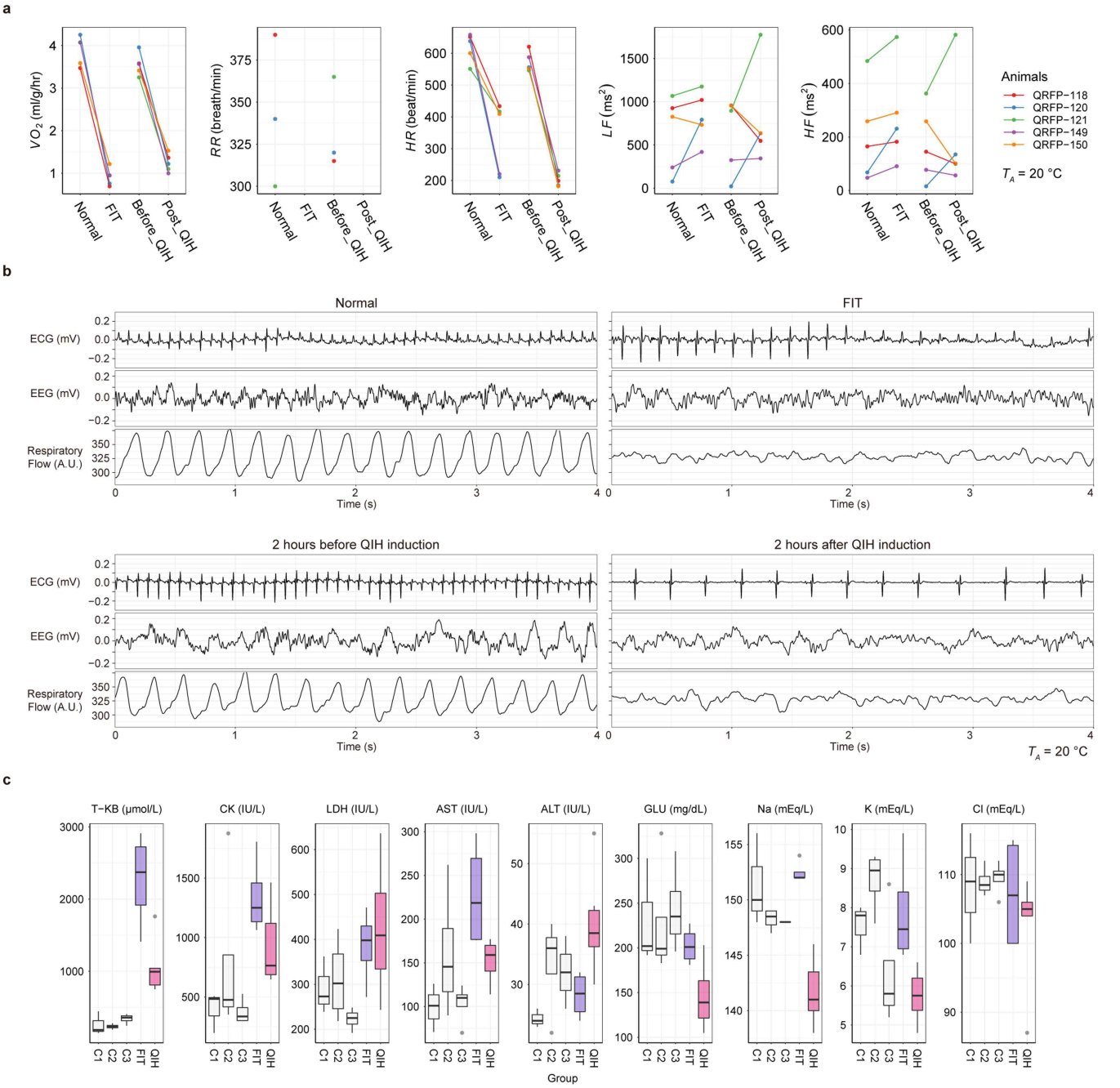

Extended Data Fig. 5 | QIH is accompanied by low heart rate, low EEG amplitude and weak respiration. ECG, EEG, VO_2 and respiratory flow were recorded during normal, FIT and QIH states ($n = 5$) in Q-hM3D mice. **a**, The one-hour median of the heart rate (HR) at minimum VO_2 during FIT was compared to that at minimum VO_2 on the day before fasting. Both VO_2 and heart rate showed marked decreases. Comparing two hours before and two hours after intraperitoneal injection of CNO, both VO_2 and heart rate were lower during QIH. The respiratory rate (RR) was undetectable in both FIT and QIH states owing to low respiratory flow. During QIH, heart rate was markedly decreased (572 and 202 beats per min, two hours before and two hours after injection of CNO, respectively). The respiratory rate of mice was reduced from 333 breaths per min to a level undetectable by the method used, suggesting that their breathing was shallow. LF and HF represent high-frequency and low-frequency power (ms^2) of HRV. **b**, Representative recordings of ECG, EEG and respiratory flow of recorded mice. Both FIT and QIH showed clear suppression of EEG amplitude. Even though movement of the chest wall was confirmed by visual inspection, respiratory flow became too low to measure the precise respiratory rate. **c**, C57BL/6J mice were fasted for 22 h from ZT0 to induce FIT ($n = 4$), followed by blood sampling at ZT22. The control group C1 ($n = 3$) was not fasted. The QIH group ($n = 6$; Q-hM3D mice) was given CNO at ZT12. Two other control groups, C2 ($n = 4$; $Qrfp^{iCre}$ mice injected with AAV_{10}-DIO-mCherry into the AVPe/MPA) and C3 ($n = 4$; Q-hM3D), were injected with saline at ZT12, followed by blood sampling at ZT22. Blood glucose levels decreased during QIH, and the QIH group of mice showed hypoglycaemia and hyponatraemia compared to control groups. Both FIT and QIH groups showed high levels of ketone bodies than control groups, although the QIH group exhibited a milder phenotype than the FIT group. Levels of aspartate aminotransferase (AST), creatine kinase (CK) and potassium were lower in QIH than in FIT. ALT, alanine transaminase; GLU, glucose; LDH, lactic acid dehydrogenase; T-KB, total ketone bodies. In the box plots, the lower and upper limits of the box correspond to the first and third quartiles; the centre line denotes the median; the upper whisker extends to the largest value that is no further than 1.5 times the interquartile range (IQR); the lower whisker extends to the smallest value that is no further than 1.5 × IQR; and the dots denote observed values that are larger or smaller than the whiskers.

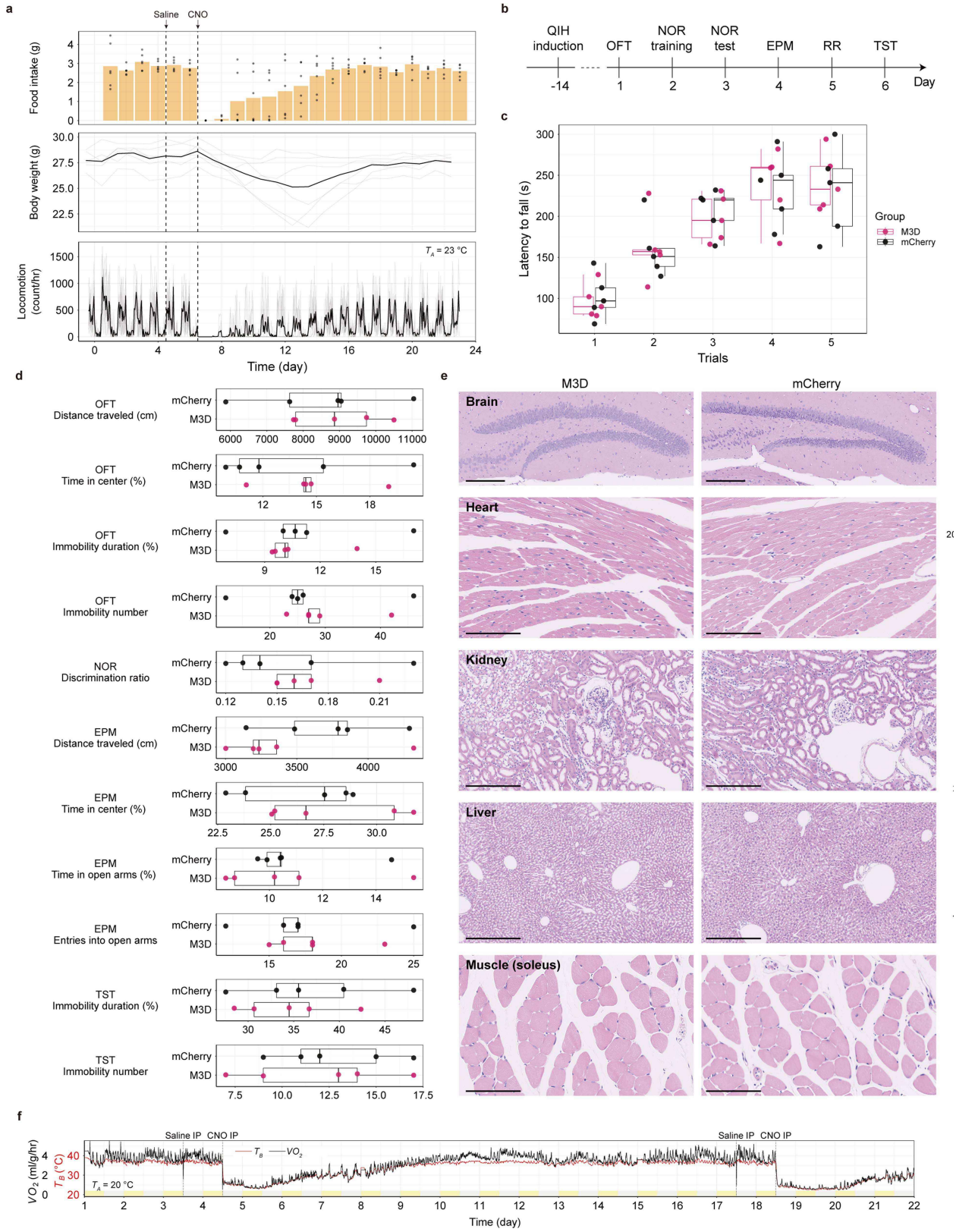

Extended Data Fig. 6 | See next page for caption.

Extended Data Fig. 6 | Mice behave normally after recovery from QIH. **a**, Food intake, body weight and activity of 6 mice were examined for 24 days before and after QIH. The first and second dashed vertical lines denote intraperitoneal injection of saline and CNO, respectively. Orange bars show the average daily food intake, and black dots represent the observed intake for each individual mouse. The bottom two panels show body weight (measured daily) and locomotor activity (measured hourly). Black lines are the average of six mice, and grey lines represent individual mice. **b**, Schematic schedule of behavioural tests. Q-hM3D mice ($n = 5$) and controls ($n = 5$; $Qrfp^{iCre}$ mice with injection of AAV_{10}-EF1α-DIO-mCherry into the AVPe/MPA) were compared. OFT, open-field test; NOR, novel object recognition test; EPM, elevated plus maze test; RR, rotarod; TST, tail suspension test. No apparent differences were observed in any behavioural tests. **c**, Results of the rotarod test. **d**, Results of the other tests. Box plots show the distribution of each group in specific tests; all elements of the box plots are as defined in Extended Data Fig. 5. **e**, Histology of tissues before and after QIH. We histologically examined whole regions in the brain, heart, kidney, liver and soleus muscles prepared from mice that did or did not experience QIH. Tissue sections were stained with haematoxylin and eosin. No gross pathophysiological changes were apparent in any of the tissues examined. Scale bars, 200 μm (brain and kidney); 100 μm (heart and soleus muscle); 400 μm (liver). **f**, Representative traces of body temperature and VO_2 during QIH, which lasts for several days and can be re-induced by another injection of CNO. Line and shading denote mean and s.d. of each group.

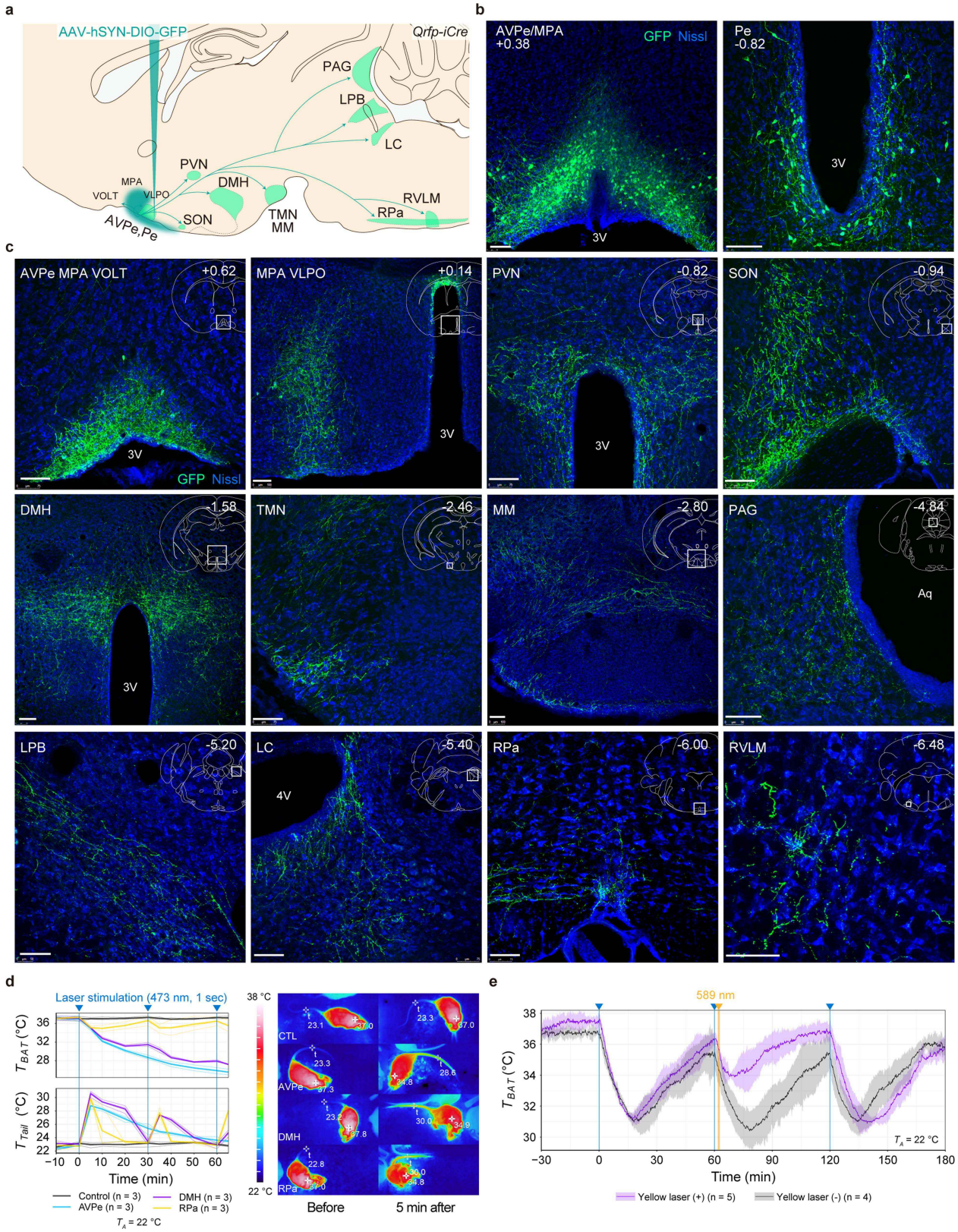

Extended Data Fig. 7 | See next page for caption.

Extended Data Fig. 7 | The DMH and RPa are major target regions for the induction of QIH. a, Strategy for delineating the axonal projection patterns of Q neurons. The neurons were visualized by injecting AAV_9-hSYN-DIO-GFP into an anteromedial hypothalamic region of *Qrfp*^{iCre} mice to express GFP in Q neurons. **b**, Distribution of GFP-positive cell bodies of Q neurons in the AVPe/MPA and periventricular nucleus. Scale bars, 100 µm. **c**, Distribution of axons arising from Q neurons. We observed GFP-positive fibres in brain regions that are implicated in the regulation of body temperature and in sympathetic regulation. Among these regions, the DMH received especially abundant projections. Aq, aqueduct; LC, locus coeruleus; LPB, lateral parabrachial nucleus; PAG, periaqueductal grey; PVN, paraventricular hypothalamic nucleus; RVLM, rostral ventrolateral medulla; VLPO, ventrolateral preoptic area; VOLT, vascular organ of the lamina terminalis; 4V, fourth ventricle. Scale bars, 100 µm. **d**, Left, temporal changes in tail temperature of Q-SSFO mice (same mice as Fig. 2c, d) after optogenetic excitation. Right, representative images of thermographs. Optogenetic focal stimulation of Q neuron axons in the RPa also induced tail vasodilation. **e**, We implanted optic fibres in the DMH of Q-SSFO mice, applied a blue laser (1-s duration) to induce QIH and then deactivated SSFO using a 589-nm yellow laser (5-s duration) to see the effect on T_{BAT}. The first shot of blue laser in DMH fibres rapidly triggers hypothermia. A sequential shot of yellow laser 3 min after the second shot of blue laser rapidly reverses the effect of the blue laser. Because deactivation of SSFO is not propagated along axons, this further supports the importance of the DMH projections of Q neurons in the induction of QIH. Lines and shading in **d**, **e** denote mean and s.d. of each group.

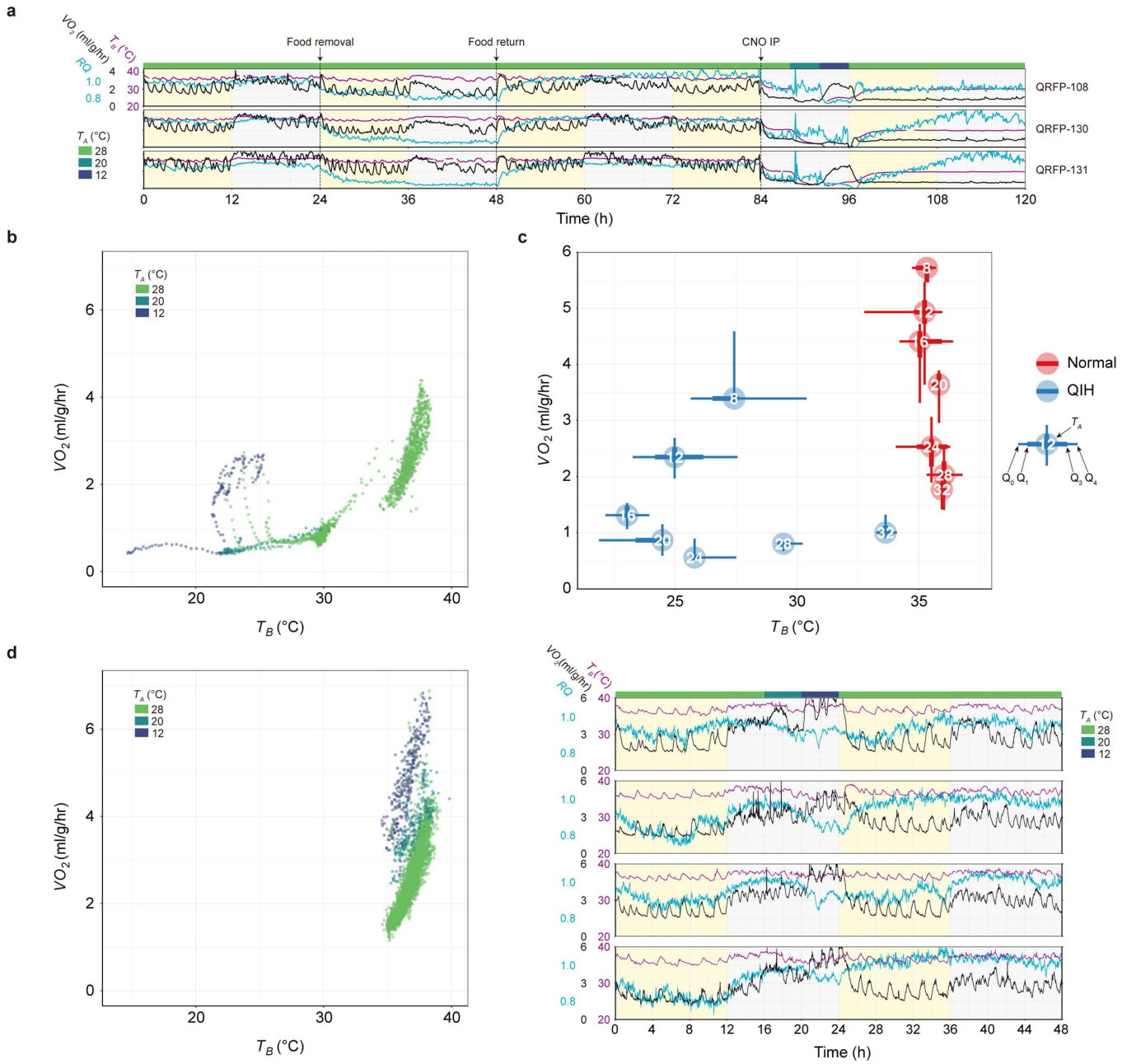

Extended Data Fig. 8 | Dynamics of set-point temperature in QIH. **a**, Transitions of metabolism when the ambient temperature was changed during QIH. See Fig. 3l for details. During QIH, when the ambient temperature was lowered from 28 °C to 20 °C, all mice showed decreased VO_2 and body temperature. By contrast, when the ambient temperature was lowered from 20 °C to 12 °C during QIH, three out of four mice showed increased VO_2 with a relatively stable body temperature. One mouse did not show an increase in VO_2, which indicates individual variance in the reduction of T_R. We confirmed that all mice spontaneously recovered from QIH. **b**, The relationship between body temperature and VO_2 during QIH with changing ambient temperature. The last 48 hours of data from Fig. 3l and **a** were merged. The colours of the dots correspond to different ambient temperatures. **c**, The relationship between the minimum body temperature and VO_2 during normal and QIH states. Data from Fig. 3b are summarized. Numbers in the dots denote the ambient temperature (°C) and the bars denote the distribution. **d**, To evaluate metabolic regulation in a normal state, wild-type C57BL/6J mice were subjected to changes in the ambient temperature. Left, the relationship between body temperature and VO_2 in all mice. Of note, body temperature is tightly controlled within a narrow range—in contrast to during QIH (**b**). Right, change in body temperature (purple), VO_2 (black) and respiratory quotient (blue) for each mouse throughout the experiment. Starting from 28 °C, the ambient temperature was lowered to 12 °C and returned to 28 °C, as shown at the top.

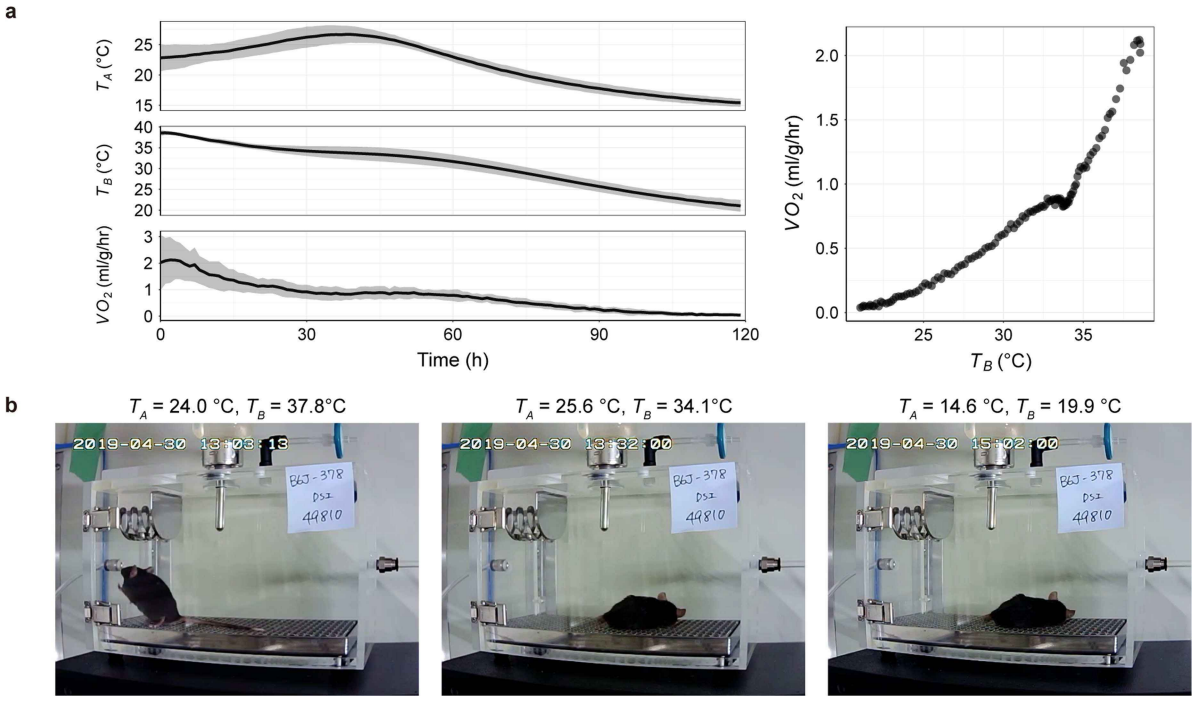

Extended Data Fig. 9 | Hypometabolism that is induced by general anaesthesia is not regulated. a, To evaluate how metabolic regulation during general anaesthesia was affected by ambient temperature, C57BL/6J mice ($n = 4$) were anaesthetized with 1% isoflurane at different ambient temperatures. Left (top row), the transition in ambient temperature. Starting from 28 °C, the set-point temperature of the chamber was lowered to 12 °C after 30 min. Because the anaesthetic machine was outside the experimental chamber and therefore the temperature of the anaesthetic gas was independent of that of the chamber, there was a delay in reaching the chamber set-point temperature. Left (middle and bottom rows), the transition in body temperature and VO_2. Both decrease along with the decrease in ambient temperature. Line and shading denote mean and s.d. Right, the relationship between body temperature and VO_2 in all mice. VO_2 did not increase in anaesthetized mice even at low body temperature, in contrast to in QIH (compare to Extended Data Fig. 8b). **b**, Representative postures of mice during anaesthesia. Left, the start of isoflurane inhalation. Middle, the start of the lowering of ambient temperature. Right, 90 minutes after the set-point temperature was lowered from 28 °C to 12 °C. No change in posture was seen even at extremely low body temperature.

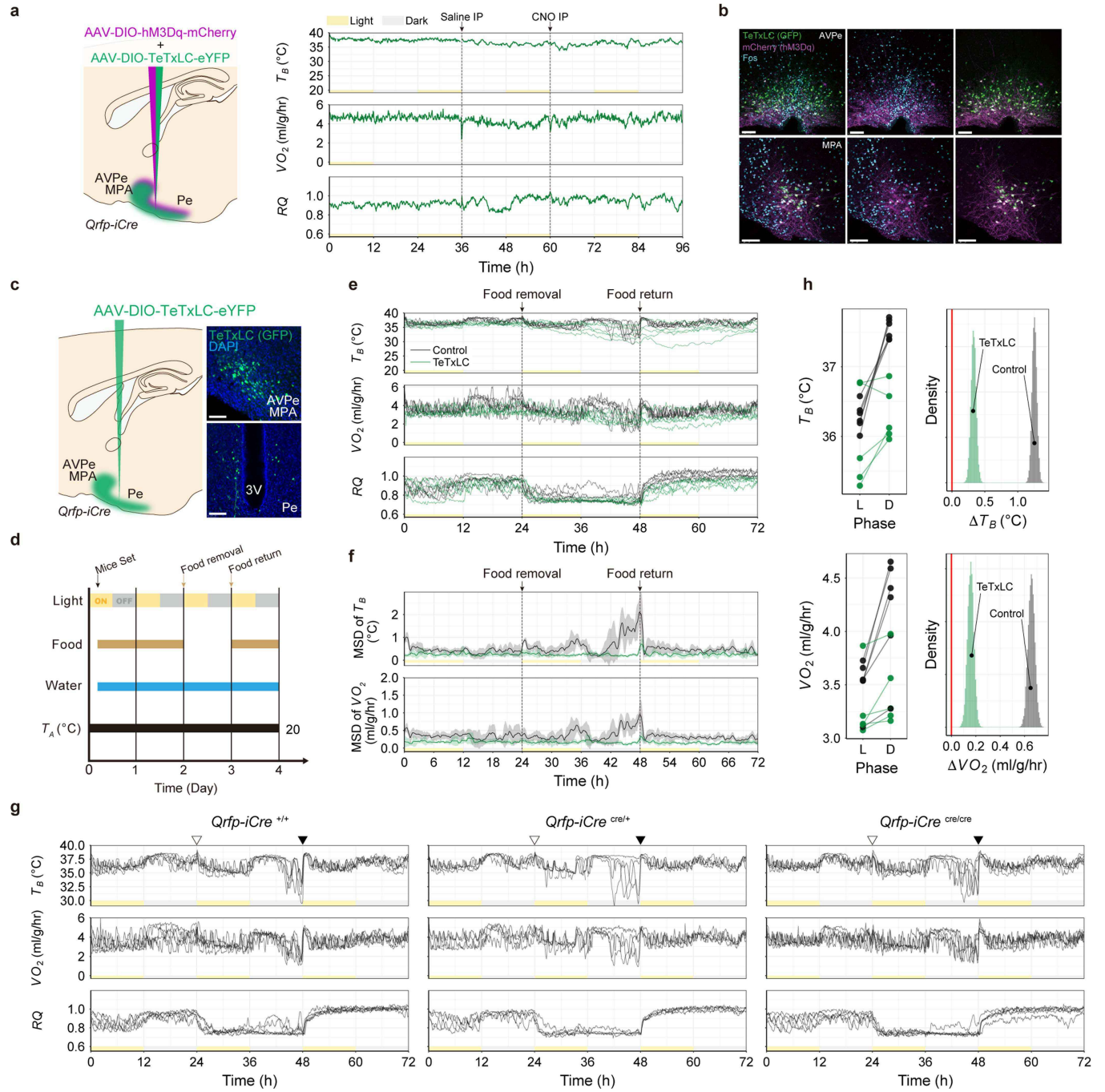

Extended Data Fig. 10 | Blocking SNARE-complex-mediated neurotransmission in Q neurons impairs daily torpor and QIH. a, CNO had almost no effect on body temperature and VO_2 in a $Qrfp^{iCre}$ mouse that was co-injected with AAV_9-DIO-hSYN-TeTxLC-eYFP and AAV_{10}-DIO-hM3Dq-mCherry into the AVPe/MPA ($n = 1$). This suggests that SNARE-mediated neurotransmission in Q neurons is indispensable for inducing QIH. **b**, Expression of TeTxLC–GFP in mCherry-positive neurons (Q neurons), shown by immunostaining 90 min after administration of CNO. Scale bar, 100 µm. **c**, Strategy for suppressing the function of Q neurons. Images show expression of TeTxLC–eYFP in the AVPe/MPA and periventricular nucleus. Scale bar, 100 µm. **d**, Schematic of FIT experiment schedule. **e**, FIT was disrupted by expressing TeTxLC in Q neurons ($n = 6$ mice for control and $n = 5$ mice for TeTxLC). The normal architecture of FIT was disrupted when neurotransmission of Q neurons was blocked in Q-TeTxLC mice. Rapid oscillatory fluctuations in metabolism were never seen in these mice. Notably, the gradual decrease in body temperature observed in these mice implies the existence of a Q-neuron-independent mechanism of metabolism reduction during FIT. **f**, The moving standard deviation (MSD; mean ± s.d.) was visualized for body temperature and VO_2 (from **e**). The low MSDs that are seen in the TeTxLC group during the fasting periods demonstrate the smaller fluctuation in this group. **g**, FIT was induced in control, $Qrfp^{iCre}$ heterozygous and $Qrfp^{iCre}$ homozygous mice, showing that the lack of QRFP peptide did not affect FIT. These observations suggest that Q neurons—but not QRFP—are an indispensable component in the induction of daily torpor, and have an important role in rapidly shifting body temperature during daily torpor. The open and closed triangles denote food removal and return, respectively. **h**, Silencing of Q neuron neurotransmission resulted in decreased circadian fluctuations in both body temperature and VO_2. The data from the first 24 h in panel **e** were divided into light (L) phase and dark (D) phase. Estimated differences in light phase and dark phase for both body temperature and VO_2 are shown as histograms of posterior distributions. Both body temperature and VO_2 showed higher values in the dark phase than in the light phase because posterior distributions are mostly positive. Although the TeTxLC group showed positive posterior distributions as well, the differences between dark phase and light phase were smaller than those in the control group. This suggests that the TeTxLC group had smaller circadian fluctuations in metabolism.

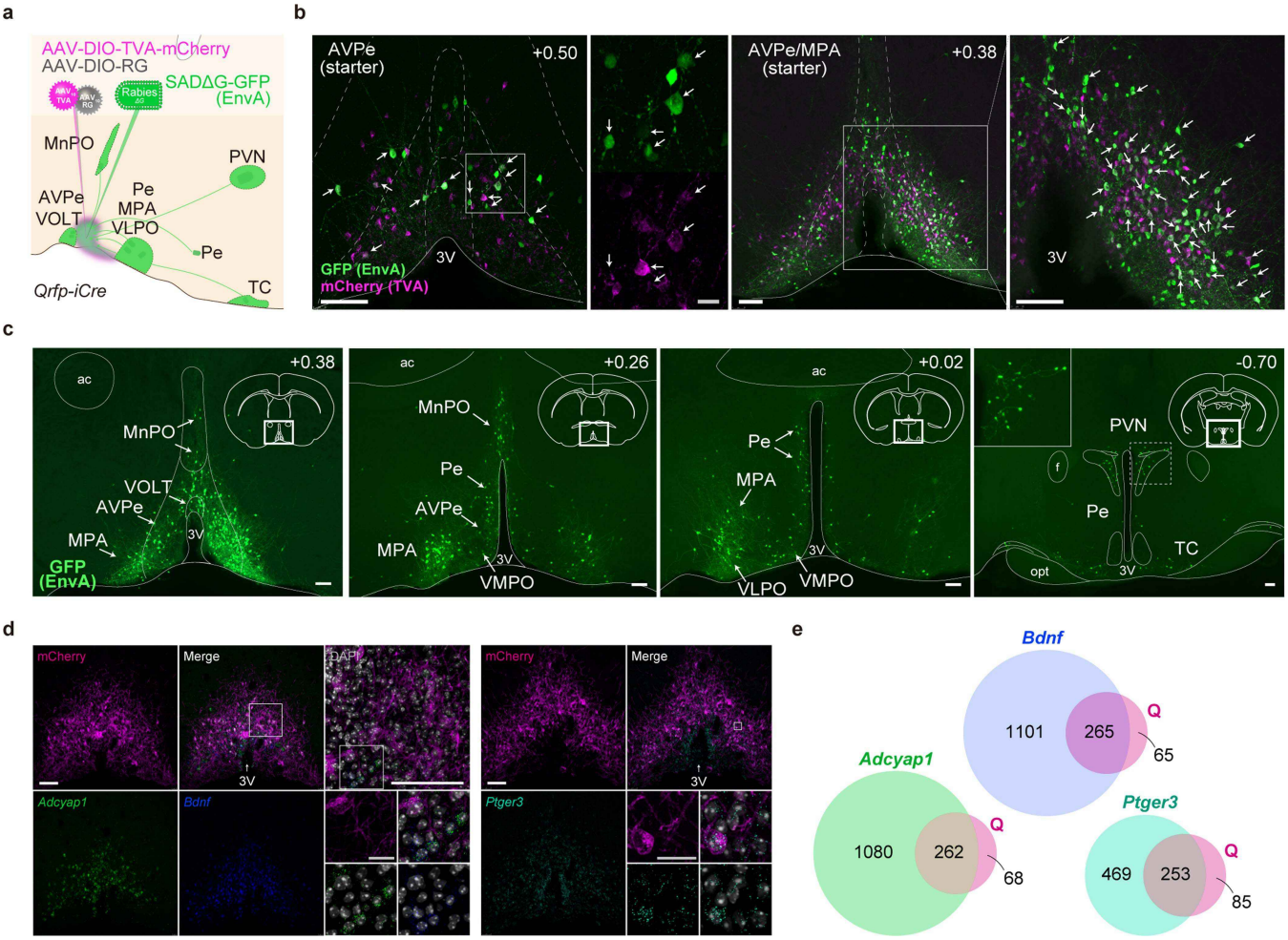

Extended Data Fig. 11 | Characteristics of Q neurons. To elucidate the possible neuronal mechanism that regulates the activity of Q neurons, we identified upstream neuronal populations that make direct synaptic contact with Q neurons by recombinant pseudotyped rabies virus vector (SADΔG(EnvA))-mediated labelling[45]. **a**, Procedure for visualizing input neurons that make mono-synaptic contact with Q neurons, using a rabies virus vector. After expressing TVA–mCherry and rabies glycoprotein (RG) in Q neurons using Cre-activatable AAV vectors[35] in *Qrfp*^{iCre} mice, we injected SADΔG-GFP(EnvA) into the AVPe/MPA. **b**, Distribution of input neurons of Q neurons. Arrows show starter cells. **c**, Brain regions that contain input neurons. Input neurons were also observed in regions in and around the AVPe and periventricular nucleus, suggesting that local interneurons exist that regulate the function of Q neurons, and also indicating that Q neurons might form microcircuitry with interneurons within the AVPe/MPA and periventricular nucleus. Our results suggest that Q neurons receive relatively sparse direct inputs from intra-hypothalamic regions. As the MPA is implicated in the regulation of body temperature[46,47], reciprocal interaction between Q neurons and the MPA might have a key role in thermoregulation. **d**, In situ hybridization in neurons immunostained for mCherry in the AVPe/MPA of Q-hM3D mice. Left, expression of *Adcyap* and *Bdnf* in Q neurons; right, expression of *Ptger3* in Q neurons. **e**, Proportions of *Adcyap*-, *Bdnf*- and *Ptger3*-positive cells in Q neurons, indicating the extent to which the Q neurons overlap with genetic markers associated with thermoregulation. Numbers show the cell counts with positive signals (two mice; three slices per mouse).

In the AVPe/MPA, mCherry-negative (non-Q) *Adcyap1*- and *Bdnf*-positive neurons were intermingled with Q neurons. Almost a quarter of *Adcyap1*- and *Bdnf*-positive neurons were Q neurons. We also found a small number of Q neurons that were negative for *Adcyap1* and *Bdnf*. These observations suggest that many Q neurons constitute a subpopulation of BDNF/PACAP neurons. Although a lot of Q neurons express *Adcyap1* and *Bdnf*, a previous report suggested that the warmth-sensing BDNF/PACAP neurons in the ventromedial preoptic area that project to the DMH are GABAergic[32]. As we found that excitatory Q neurons have a major role in inducing QIH (Fig. 4), Q neurons apparently constitute a unique, previously unidentified population among the group of preoptic-area neurons that are involved in thermoregulation. Notably, we found that many Q neurons express both *Vgat* and *Vglut2* (Q_H neurons) (Fig. 4a). This is consistent with a previous study reporting that many BDNF/PACAP neurons in the preoptic area express both *Vgat* and *Vglut2*[24], because Q neurons are a subset of BDNF/PACAP neurons. Prostaglandin EP3 receptor (*Ptegr3*), which is implicated in causing fever[16,48], is expressed in Q neurons. Again, the number of *Ptegr3*-positive neurons was larger than that of Q neurons, but three quarters of Q neurons expressed *Ptegr3*. This suggests that PGE2 inhibits Q neurons through acting on EP3 in Q neurons, although our inhibitory DREADD experiments did not show any effects on T_{BAT} (Extended Data Fig. 2c). ac, anterior commissure; f, fornix; MnPO, median preoptic area; opt, optic tract; VLPO, ventrolateral preoptic area; VMPO, ventromedial preoptic area.

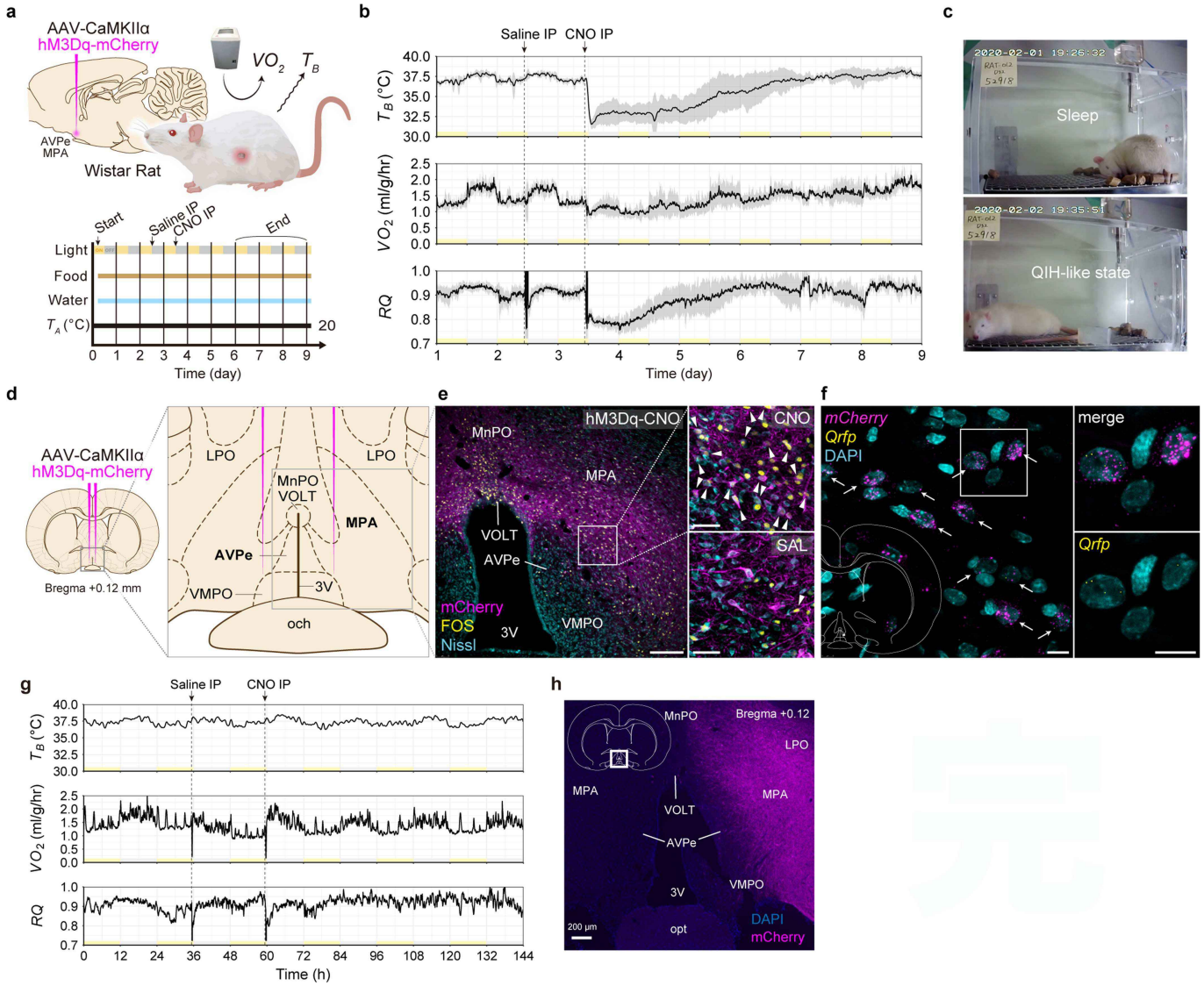

Extended Data Fig. 12 | Induction of a QIH-like state in rats. a, Procedure for the metabolic analysis with chemogenetic activation of AVPe/MPA neurons in rats. Saline and CNO were administered just before the beginning of the dark phase. Recordings were taken until the metabolism recovered to baseline levels. **b**, Activating AVPe/MPA neurons, including Q neurons in rats, induced a QIH-like state of hypothermia and hypometabolism ($n = 7$). The lines and shadings denote mean and s.d. Body temperature, VO_2 and the respiratory quotient remained low for more than 24 h after intraperitoneal injection of CNO, as in mice during QIH, and then spontaneously returned to normal states. **c**, Representative images showing the typical posture of rats during a QIH-like state compared with during sleep. **d**, Schematic drawing of virus (AAV_{10}-CaMKIIα-hM3Dq-mCherry) injections into the AVPe/MPA of the rat brain. Stereotaxic brain maps are based on Paxinos and Watson's atlas[39]. The grey rectangular region in the right panel shows the area in which the following histological evaluations are focused. **e**, Distribution of hM3Dq-mCherry-expressing neurons in the AVPe/MPA. Arrowheads indicate hM3Dq-expressing neurons that are positive for FOS immunofluorescence 90 min after intraperitoneal injection with CNO or saline. Scale bars, 200 μm (left), 50 μm (right). **f**, *Qrfp* and *mCherry* transcripts detected in the AVPe/MPA of rats. Arrows denote co-expression of *Qrfp* and *mCherry* mRNAs. Scale bars, 10 μm. **g**, Body temperature, VO_2 and respiratory quotient before and after CNO injection in rat no. 014, which did not show a QIH-like state. **h**, Expression of hM3Dq-mCherry in the AVPe/MPA region of rat no. 014. We observed unilateral expression of hM3Dq-mCherry in the MPA region. This suggests that bilateral proper expression of hM3Dq in the AVPe/MPA is necessary to evoke the QIH-like state. Collectively, seven out of eight rats showed a QIH-like state, characterized by a prominent decrease in body temperature. In these rats, the reduction in body temperature was accompanied by a decrease in VO_2, a lowered respiratory quotient and an extended posture, showing further similarity with the QIH state in mice. The efficiency of induction of a QIH-like state in these rats is likely to be lower than that in Q-hM3D mice, owing to ectopic expression of hM3Dq in non-Q neurons within and around the AVPe/MPA.

nature research

Corresponding author(s): Takeshi Sakurai, Genshiro A. Sunagawa

Last updated by author(s): Dec 10, 2019

Reporting Summary

Nature Research wishes to improve the reproducibility of the work that we publish. This form provides structure for consistency and transparency in reporting. For further information on Nature Research policies, see Authors & Referees and the Editorial Policy Checklist.

Statistics

For all statistical analyses, confirm that the following items are present in the figure legend, table legend, main text, or Methods section.

n/a	Confirmed	
☐	☒	The exact sample size (*n*) for each experimental group/condition, given as a discrete number and unit of measurement
☐	☒	A statement on whether measurements were taken from distinct samples or whether the same sample was measured repeatedly
☒	☐	The statistical test(s) used AND whether they are one- or two-sided *Only common tests should be described solely by name; describe more complex techniques in the Methods section.*
☒	☐	A description of all covariates tested
☒	☐	A description of any assumptions or corrections, such as tests of normality and adjustment for multiple comparisons
☐	☒	A full description of the statistical parameters including central tendency (e.g. means) or other basic estimates (e.g. regression coefficient) AND variation (e.g. standard deviation) or associated estimates of uncertainty (e.g. confidence intervals)
☒	☐	For null hypothesis testing, the test statistic (e.g. *F*, *t*, *r*) with confidence intervals, effect sizes, degrees of freedom and *P* value noted *Give P values as exact values whenever suitable.*
☐	☒	For Bayesian analysis, information on the choice of priors and Markov chain Monte Carlo settings
☒	☐	For hierarchical and complex designs, identification of the appropriate level for tests and full reporting of outcomes
☒	☐	Estimates of effect sizes (e.g. Cohen's *d*, Pearson's *r*), indicating how they were calculated

Our web collection on statistics for biologists contains articles on many of the points above.

Software and code

Policy information about availability of computer code

Data collection	InfReC Analyzer NS9500 Professional software (NIPPON AVIONICS); Ponemah Physiology Platform (version 6.30, DSI); AD converter (Biotex); mass spectrometer(ARCO-2000 , ARCO System); LAS X 3.1.1.157512 for Leica TCS SP8 confocal microscope; ZEN 2.3 for Zeiss Axio Zoom.V16 microscope.
Data analysis	Every analysis and chart output was produced by R (version 3.52 or above). Every script for Bayesian inference is available on web.

For manuscripts utilizing custom algorithms or software that are central to the research but not yet described in published literature, software must be made available to editors/reviewers. We strongly encourage code deposition in a community repository (e.g. GitHub). See the Nature Research guidelines for submitting code & software for further information.

Data

Policy information about availability of data

All manuscripts must include a data availability statement. This statement should provide the following information, where applicable:

- Accession codes, unique identifiers, or web links for publicly available datasets
- A list of figures that have associated raw data
- A description of any restrictions on data availability

Included in main text.

Field-specific reporting

Please select the one below that is the best fit for your research. If you are not sure, read the appropriate sections before making your selection.

☒ Life sciences ☐ Behavioural & social sciences ☐ Ecological, evolutionary & environmental sciences

For a reference copy of the document with all sections, see nature.com/documents/nr-reporting-summary-flat.pdf

Life sciences study design

All studies must disclose on these points even when the disclosure is negative.

Sample size	No statistical method was used to determine the sample size for the animal experiments. The number of animals recorded in one group (i.e. QIH induction at 24 °C of ambient temperature) was chose based on previous experience and standards in this field. Sample sizes were described in the manuscript.
Data exclusions	We excluded mice heavier than 34 g in daily torpor experiments (Extended Data Fig.8e-h) because we found that mice weighing over 34 g did not reproducibly exhibit FIT. This criteria was not pre-specified. In the QIH-like state induction in rats (Extended Data Fig.12b), we excluded a rat which did not show expression of mCherry in the AVPe/MPA bilaterally (the data is shown in Extended Data Fig.12g, h).
Replication	See "Statistics and reproducibility"
Randomization	Because the animal we have used in this study were all inbred strains, we did not randomize the animals within a strain.
Blinding	Blinding was not performed in this study in animal experiments because nearly all data acquisition was automated and therefore have high objectivity. The histology study was not blinded due to simple human resource issue.

Reporting for specific materials, systems and methods

We require information from authors about some types of materials, experimental systems and methods used in many studies. Here, indicate whether each material, system or method listed is relevant to your study. If you are not sure if a list item applies to your research, read the appropriate section before selecting a response.

Materials & experimental systems

n/a	Involved in the study
☐	☒ Antibodies
☒	☐ Eukaryotic cell lines
☒	☐ Palaeontology
☐	☒ Animals and other organisms
☒	☐ Human research participants
☒	☐ Clinical data

Methods

n/a	Involved in the study
☒	☐ ChIP-seq
☒	☐ Flow cytometry
☒	☐ MRI-based neuroimaging

Antibodies

Antibodies used	Commercially available antibodies were used. Primary antibodies used in the study were: rabbit anti-cFos (1:4000, ABE457, Millipore); goat anti-mCherry (1:15000, AB0040-200, Sicgen); rat anti-GFP (1:5000, 04404-84, Nacalai Tesque); mouse anti-TH (1:1000, sc-25269, Santa Cruz Biotechnology); mouse anti-orexin-A (1:200, sc-80263, Santa Cruz Biotechnology); and rabbit anti-MCH (1:2000, M8440, Sigma). Secondary antibodies used were: donkey anti-rabbit, goat, rat, or mouse, conjugated with Alexa 488, 594 or 647 (A21206, A21208, A11037, A11058, A31573, A31571, all 1:1000, all purchased from Invitrogen).
Validation	All antibodies were commercial in origin. Validation statements can be found on the manufacturer's website as following. Rabbit anti-cFos (ABE457, Millipore): https://www.merckmillipore.com/JP/ja/product/Anti-c-Fos-Antibody,MM_NF-ABE457 Goat anti-mCherry (AB0040-200, Sicgen): https://www.labome.com/product/SICGEN/AB0040-200.html Rat anti-GFP (04404-84, Nacalai Tesque): https://www.labome.com/product/Nacalai-Tesque/04404-84.html Mouse anti-TH (sc-25269, Santa Cruz Biotechnology): https://www.scbt.com/p/th-antibody-f-11 Mouse anti-orexin-A (sc-80263, Santa Cruz Biotechnology): https://www.scbt.com/ja/p/orexin-a-antibody-kk09 Rabbit anti-MCH (M8440, Sigma): https://www.sigmaaldrich.com/catalog/product/sigma/m8440?lang=ja&region=JP In the present study, validation was performed in our laboratory, testing on mouse and/or rat brain tissues.

Animals and other organisms

Policy information about studies involving animals; ARRIVE guidelines recommended for reporting animal research

Laboratory animals	We used C57BL/6J mice and Wister rats. Except during torpor-inducing experiments, animals were given food and water ad libitum and maintained at TA of 23 °C at IIIS and 22 °C at BDR, relative humidity of 50%, with a 12-hr light/12-hr dark cycle. Qrfp-iCre mice were generated by homologous recombination in C57BL/6N embryonic stem cells and implantation in 8-cell-stage embryos (ICR). A targeting vector was designed to replace the entire coding region of the prepro-Qrfp sequence in exon 2 of the Qrfp gene with iCre and pgk-Neo cassette so that the endogenous Qrfp promoter drives expression of iCre (Extended Data Fig. 1). Chimeric mice were crossed with C57BL/6J females (Jackson Labs). The Pgk-Neo cassette was deleted by crossing them with FLP66 mice, which had been backcrossed to C57BL/6J mice at least 10 times. Initially, F1 hybrids from mating heterozygotes with heterozygotes were generated. We backcrossed them to C57BL/6J mice at least 8 times. All experiments were performed on iCre heterozygotes, unless indicated otherwise. Rosa26dreaddm3 and Rosa26dreaddm4 mice were generated by homologous recombination in C57BL/6N embryonic stem cells, followed by the same procedure as in Qrfp-iCre mice described above. Targeting vectors are shown in Extended Data Fig. 2a. Slc32a1tm1Lowl (referred to as Vgatflox/flox) mice and Slc17a6tm1Lowl (Vglut2flox/flox) mice were obtained from the Jackson Laboratory (Stock No: 012897 and 012898, respectively). Wistar rats were purchased from Oriental Yeast Co., Ltd. Male mice with ages ranged from 8 to 20 weeks old. Male rats were used in 8 - 11 week old.
Wild animals	No wild animal used in this study.
Field-collected samples	No samples collected at the field in this study.
Ethics oversight	All animal experiments were performed at the International Institute of Integrative Sleep Medicine (IIIS), Tsukuba University and RIKEN Center for Biosystems Dynamics Research (BDR), according to their guidelines for animal experiments. They were approved by the animal experiment committees of each institute, and thus were in accordance with NIH guidelines.

Note that full information on the approval of the study protocol must also be provided in the manuscript.